
Modelling of composite fin-plate connections under fire conditions using component-based method

Guan Quan¹, Xu Dai^{2*}, Jun Ye³, Shan-Shan Huang⁴, Ian Burgess⁴

¹ Department of Civil Engineering and Surveying, University of Portsmouth, Portland Building, Portland Street, Portsmouth PO1 3AH, UK

² Fire Engineering, Buro Happold, Newman Street, London W1T 1PD, UK

³ Department of Civil and Environmental Engineering, University of Strathclyde, Glasgow, UK

⁴ Department of Civil and Structural Engineering, University of Sheffield, Sir Frederick Mappin Building, Mappin Street, Sheffield S1 3JD, UK

Abstract

Composite floor systems with fin-plate connections are widely used in multi-storey buildings, but there is currently no reported research on the development of a component-based model of a fin-plate connection at the beam-column interface that includes the effect of slab continuity above the fin-plate connection. In this research, a component-based model is developed to simulate a composite fin-plate connection. The component-based composite fin-plate connection model is able to simulate the slab continuity when installed at the beam-to-column interface of a composite floor system model. Fracture criteria for the plates and bolts of the fin-plate connection are adopted in the model to simulate connection failure. The component-based composite fin-plate connection model has been implemented in the software Vulcan, and is validated against a range of existing results, covering tests of individual fin-plate connections at ambient and constant high temperatures, subjected to combinations of tensile force, shear force and moment. The

element is also used to simulate a test in which fin-plate connections were implemented at both ends of a composite beam with slab continuity, and subjected to elevated temperatures. The Vulcan modelling results show good comparison with the test results. The proposed component-based composite fin-plate connection model is shown to be a reliable tool to enable the performance-based finite element modelling of full-scale composite beams with fin-plate connections under fire conditions. Subsequently, parametric studies are carried out to investigate the influence of the key parameters, axial restraint stiffness and reinforcement ratio, on the behaviour of the composite beam and the connection force distribution, as well as to compare the very dissimilar structural responses of bare-steel and composite beams with the same geometries and loading conditions in fire.

Key Words: fin-plate connection, composite beam, fire, component-based model

Introduction

Beam-to-column connections may often be the most crucial part of a structure under fire conditions. This is because connections provide links between different structural members and are vulnerable to failure in fire [1]. The failure of connections may trigger the collapse of floors or even progressive collapse of a whole building [2]. Depending on their design assumptions, connections should be designed to resist shear force and/or bending moment at ambient temperature. According to the current code of practice, Eurocode 3 [3], connections are designed to achieve this criterion at ambient temperature. However, Eurocode 3 then assumes that the designed connection is also sufficient at elevated temperatures, provided that (i) the fire protection on the connection is equal or greater than that on the connection members and (ii) the utilization of the connection is equal or less than the maximum value of utilization of any of the connected

members [4]. Eurocode 3 also recommends an alternative method to determine the fire resistance of joints by designing the bolts and/or the welds, considering the material reduction factors and partial factor under fire conditions. No approach has been provided in Eurocode 3 to design the connections, as a whole, which deals with realistic loading combinations, large deformation, and potential fracture of connections at high temperature.

Full-scale fire tests at Cardington [5, 6] and NIST [7] demonstrated that the behaviour of a composite steel framed structure under fire conditions can be completely different from that of isolated members seen in conventional furnace fire testing. In such full-scale fire tests, it is found that connections are subject to high compressive forces due to the restraint of thermal expansion of their adjacent beams [1]. At a later stage, connections are subject to large tying forces due to the development of catenary action when the connected beams experience large deflection and lose the majority of their bending strength and stiffness at very high temperatures [8, 9]. Therefore, connections should be designed with sufficient rotational capacity as well as compressive and tensile resistances, considering the complicated combinations of forces, as mentioned above. To do so, firstly, it is essential to understand the behaviour of an individual connection subject to all possible forces produced by the adjacent structural members. Secondly, it is ideal to evaluate, experimentally and/or numerically, the connection behaviour within a full-scale structure subject to fire.

Carrying out full-scale fire tests for all the structural frames is impractical due to their high costs. Conducting full-scale numerical frame modelling at elevated temperatures via detailed finite element (FE) analysis requires extremely high computational costs. One practical alternative is to implement component-based model to FE analysis, using which to carry out performance-based structural fire engineering design. In the component-based method, a connection is considered as an assembly of nonlinear springs, instead of being

modelled in detail using solid elements. Each of the spring has its individual characteristic and temperature. The key behaviour of the connection can be reflected with reasonable accuracy by assembling these nonlinear springs into a connection element. This significantly reduces the degrees of freedom implemented into the numerical model, thus considerably improves the computational efficiency [10]. By using the component-based method, it is possible to include connections in the simulation of full-scale structures in fire. This helps to investigate the connection behaviour while fully considering the complexity of forces applied onto connections, as well as to investigate the influence of connections on the structural response of full-scale frames in fire. The component-based modelling approach is theoretically applicable to any FE software that is capable of accepting user-defined characteristics for an assembly of springs, to simulate the behaviour of connections under various combinations of loads in fire. However, since the majority of commercial finite element software, such as ABAQUS and ANSYS, do not have this as a standard function, researchers tend to develop their own FE software to realize the application of the component-based method. One example is the software Vulcan [11].

Vulcan [11] is a three-dimensional FE software developed by the Fire Engineering Research Group at the University of Sheffield, allowing engineers to conduct performance-based three-dimensional frame analysis under fire conditions. A variety of element types, including beam-column [12, 13], slab [14, 15], shear connector [16] and connection elements [17, 18], have already been developed in Vulcan. The connection element of Vulcan is based on component-based method and covers different types of connections, such as idealised pinned, idealised rigid, end plate, fin-plate and reverse channel connections.

In the structural integrity test (No.7) of the full-scale Cardington Fire Tests on an eight-storey composite steel-framed building, fin-plate connections were used to connect the secondary beams to the primary beams [5].

Sarraj [19] simulated this test series via three-dimensional FE modelling with ABAQUS [20] to investigate the behaviour of fin-plate connections at ambient temperature and elevated temperatures. Sarraj [19] then proposed a component-based model of bare-steel fin-plate connection, which included a plate bearing component, a bolt-in-single-shear component and a friction component. Hu [21] carried out tests on fin-plate connections subjected to axial tension force and inclined tension force at high temperatures. A detailed fin-plate connection FE model was developed using ABAQUS and validated against tests. Subsequently, sub-frame models, including a steel beam and detailed connection model at beam ends, were developed to gain further insights into the behaviour of fin-plate connections in fire. Yu et al. [22] performed tests on fin-plate connections subject to combined shear, tension and bending moment at ambient and elevated temperatures. Yu et al. [21] simulated their tests using Sarraj's component-based model and obtained a good match. Taib [23] further developed Sarraj's component-based model by amending the friction component, and integrated it into Vulcan as a fin-plate connection element. Taib [22] verified the fin-plate connection element of Vulcan against Yu's tests and then carried out a series of parametric studies to investigate the bolt row force distribution within a fin-plate connection in a steel frame, as well as the behaviour of sub-frames with fin-plate connections at elevated temperatures. Despite the tremendous efforts of previous researchers on understanding the behaviour of fin-plate connections under fire conditions and on developing a tool (component-based model) to carry out performance-based design with fin-plate connections, the existing fin-plate component-based models are not applicable to a composite beam/floor system, as they cannot simulate slab continuity.

Fin-plate connections are widely used in composite floors. Selden et al. [24] carried out tests on composite beams subject to constant heating rate, three of which had fin-plate connections at the beam ends. The

detailed connection responses of the same tests were reported by Fischer et al. in a later paper [25]. These tests provided useful data for specimens designed according to U.S. standards, and can be used to validate numerical modelling techniques. However, due to the laboratory space limitation, the test beams were of short (3.81m) spans, whereas the span of composite beams is usually more than 7.5m in engineering practice. Moreover, the slab continuity was not reflected in the test setup; the connections were non-composite; and the loading and heating parameters were limited in the tests. Being fully aware of the experimental limitations, Fischer and Varma [26] conducted parametric studies via detailed FE analysis using the software ABAQUS. The influence of various geometric detailing, fire loading and fire protection parameters were evaluated. The authors also developed a three-bay model, with fire in the middle bay, to evaluate the effects of the continuous slab as well as the effects of the restraints from the surrounding cooler structures under fire conditions. It was pointed out by Fischer and Varma [26] that such detailed numerical analyses of large models required specific computational equipment when executing and post processing the analyses. Therefore, it is still important to develop the component-based approach to simulate connections, in order to carry out high-temperature full-scale structural frame analysis while keeping the computational costs at a generally accessible level.

Yotsumoto et al. [27] conducted high-temperature tests on three beams of 6m span with fin-plate connections; one steel beam, one composite beam without slab continuity and one composite beam with slab continuity. The effects of the hogging moment resistance of fin-plate connections on the failure time of the beams were investigated. This facilitated the development of a simplified design method of steel/composite beams of fin-plate connections. Ramesh et al. [28], and Choe et al. [29] carried out four tests of composite long (12.8m) span beams with fin-plate connections or double angle connections at the beam

ends. One of the four tests considered slab continuity by anchoring the steel reinforcements of the slab to the supporting column. The tests provided valuable experimental data for the validation of numerical modelling. Dai et al. [7] reported a full-scale fire test on a 3 x 2 bay two-story steel frame with composite floors and fin-plate connections. The test significantly enriched the experimental data library of the thermal and structural responses of composite beams with fin-plate connections to a full-scale large compartment fire, considering the restraints from adjacent cold structures. This study identifies the importance of considering realistic axial load and rotational demand on fin-plate connections, due to the thermal elongation or contraction of composite beams, in future structural fire design guidance.

In this research, a component-based model representing fin-plate connections in a composite beam/floor system (called composite fin-plate connection hereafter) has been developed for both ambient and elevated temperatures, for the first time. The component-based composite fin-plate connection model is able to simulate the slab continuity in a composite beam/floor system. Fracture criteria for the plates and bolts of the fin-plate connections have been adopted in the model to simulate connection failure. This composite fin-plate connection model is integrated into the FE software Vulcan as a composite fin-plate connection element, and has been validated against experimental results. The proposed component-based composite fin-plate connection model has been proven to be a reliable tool to enable the performance-based finite element modelling of composite frames with fin-plate connections under fire conditions. Subsequently, the structural responses of bare-steel and composite fin connections are compared. Parametric studies are also carried out to investigate the influence of key parameters (axial restraint stiffness and reinforcement ratio) on the behaviour of composite beams and on the connection force distributions.

1 Component-based composite fin-plate connection element in Vulcan

The component-based model of composite fin-plate connections is composed of nonlinear springs that represent the different components within the connection. Each spring has its individual characteristics, and deforms independently under tension and/or compression. The overall performance of the connection can be simulated by the assembly of these springs. In this section, the development of the component-based composite fin-plate connection model is introduced. An example model of a three-bolt row composite fin-plate connection is shown in Figure 1.

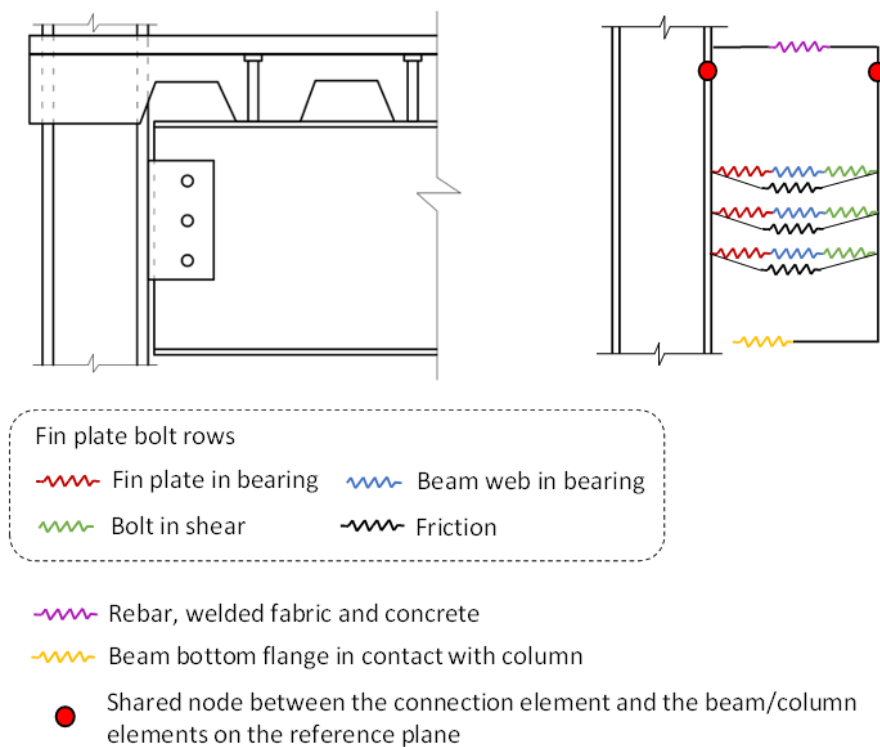


Figure 1. Component-based model for a three-bolt row composite fin-plate connection

The connection model is composed of three parts: a spring representing the concrete flange containing rebars, springs representing the bolt rows of the fin-plate connection and a spring representing the beam bottom flange in contact with the column. Each bolt row of the fin-plate connection is simulated by four

springs. Three of these four springs, representing fin-plate in bearing, bolt in shear and beam web in bearing, are in series. This series of three springs is in parallel with the fourth spring, which simulates the friction between the bolt nut and the contacted plate. It is assumed that the connection element has infinite stiffness in the vertical direction. This is because a variety of studies [1, 5, 30] have observed that the design vertical shear force carried by a connection is much lower than its horizontal force at high temperatures. Therefore, the fin-plate connection tends to fail due to excessive horizontal force and rotation prior to failure due to loss of vertical shear capacity. Each nonlinear spring is able to deal with unloading and displacement reversal, during which the spring force-deformation relationship in unloading does not simply reverse its loading route. The detailed analytical procedure of unloading and displacement reverse follows the same principle as described by Block et al. [17]. The mechanical models of all the nonlinear springs are described in the sections below.

1.1 Concrete flange containing rebars

The spring, representing the concrete flange of the composite beam, accounts for the contribution of the rebars embedded in concrete. This spring itself forms the top spring row. It is assumed that this spring locates at the centre line of the rebars. The spring could be under tension or compression, depending on the combined effect of the hogging moment at beam ends and the compression due to restrained thermal expansion.

When the spring is under compression, the rebars work together with the concrete. It is assumed that the concrete flange is uniformly compressed, and the stiffness of this spring under compression K_{RC} can be calculated according to Eq. (1):

$$K_{RC} = (E_{c,\theta} t_c b_c + E_{r,\theta} A_r) / L_b \quad (1)$$

where, $E_{c,\theta}$ is the temperature-dependent elastic modulus of concrete; $E_{r,\theta}$ is the temperature-dependent elastic modulus of rebars; t_c is the nominal thickness of concrete flange; b_c is the width of concrete flange, A_r is the overall area of the rebars, and L_b is the length of composite beam. It is assumed that the compression force in the concrete flange is small enough for the concrete to remain linear elastic (as observed in experiments [31]), and so Eq.(1) remains valid as load or temperature increases.

When the spring is under tension, the rebars contribute to the tensile resistance of the spring, whereas concrete in tension is ignored. The bilinear rebar pull-out model developed by Sezen and Setzler [32] has been employed. The stress-strain relationship of the rebars is illustrated in Figure 2 (a). $f_{yr,\theta}$ is the rebar yield stress; $f_{sr,\theta}$ is the rebar stress; $f_{ur,\theta}$ is the rebar ultimate strength; $\varepsilon_{yr,\theta}$ is the rebar yield strain; $\varepsilon_{sr,\theta}$ is the rebar strain; and $\varepsilon_{ur,\theta}$ is the rebar ultimate strain. The reduction factors for reinforcing steel recommended by Eurocode 4 [33] are applied to the yield stress, ultimate strength and elastic modulus of the rebars to account for the degradation of the material at high temperature.

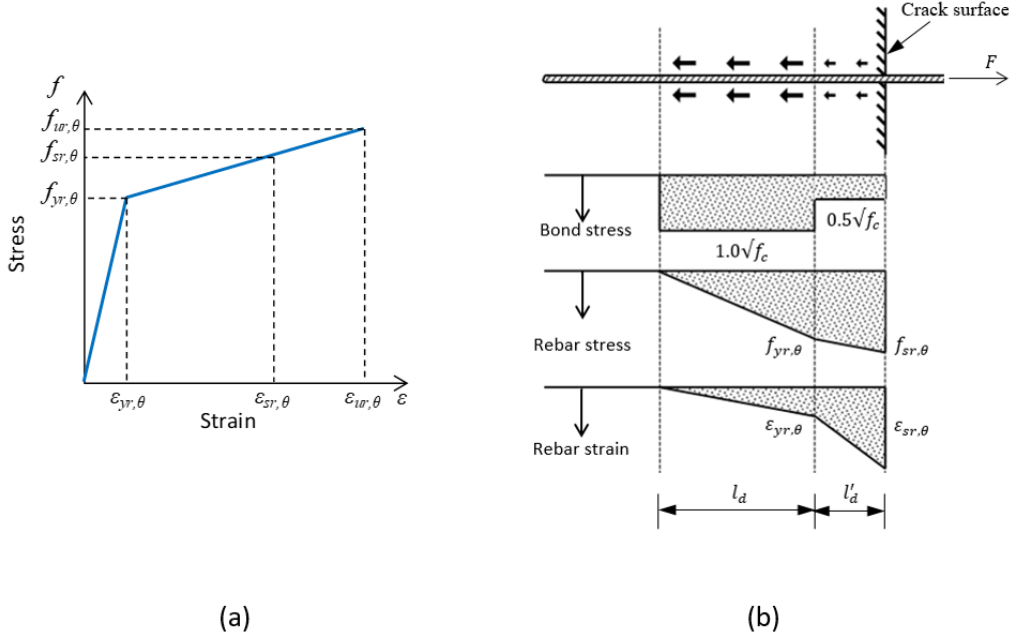


Figure 2. Sezen and Setzler model for reinforcement bar bond, stress and strain [32]

When the rebars are pulled from the concrete, the concrete cracks due to its low tensile resistance. Within the crack zone, the bond stress between the concrete and the rebar is neglected. Out of the crack zone, the rebars are embedded in the concrete flange; the bond stress between the rebars and concrete prevents the rebars from being pulled out. The bond stress u'_b close to the crack surface is assumed to be constant at $0.5\sqrt{f_c}$ for a length of l'_d . Within this area, the rebar stress and strain are assumed to be distributed linearly, as shown in Figure 2 (b). The rebar stress is between $f_{yr,\theta}$ and $f_{sr,\theta}$, and the rebar strain is between $\epsilon_{yr,\theta}$ and $\epsilon_{sr,\theta}$. The bond stress u_b further away from the crack surface is assumed to be constant at $1.0\sqrt{f_c}$ for a length of l_d . Within this area, it is assumed that the rebar stress and strain distributed linearly from 0 to $f_{yr,\theta}$ and $\epsilon_{yr,\theta}$, respectively. f_c is the compressive strength of concrete at ambient temperature. l_d and l'_d can be calculated as:

$$l_d = f_{yr,\theta} d_r / 4u_b \quad (2)$$

$$l'_d = (f_{yr,\theta} - f_{sr,\theta})d_r/4u'_b \quad (3)$$

where, d_r is the diameter of the rebar.

The total slip from the crack surface can be calculated as:

$$slip = \varepsilon_{yr,\theta}l_d/2 + (\varepsilon_{yr,\theta} + \varepsilon_{sr,\theta}) l'_d/2 \quad (4)$$

The force-deformation relationship of the rebar spring in tension is illustrated in Figure 3.

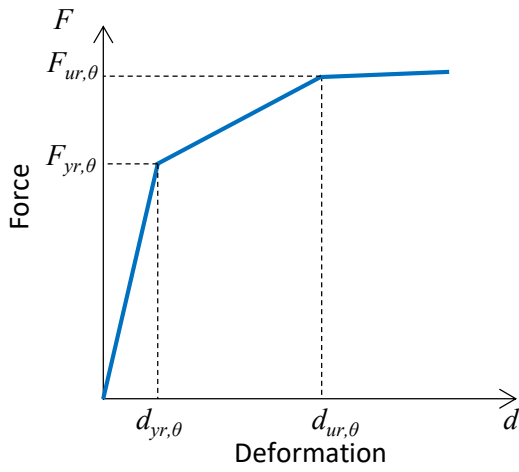


Figure 3. Force-deformation relationship of the rebar spring

The critical points of this curve are calculated according to Eqns. (5)-(8).

$$F_{yr,\theta} = f_{yr,\theta}A_r \quad (5)$$

$$F_{ur,\theta} = f_{ur,\theta}A_r \quad (6)$$

$$d_{yr,\theta} = \varepsilon_{yr,\theta}l_d/2 + \varepsilon_{yr,\theta}l'_d \quad (7)$$

$$d_{ur,\theta} = \varepsilon_{yr,\theta}l_d/2 + (\varepsilon_{yr,\theta} + \varepsilon_{ur,\theta}) l'_d/2 \quad (8)$$

in which $F_{yr,\theta}$ is the temperature-dependent yield force of the concrete containing rebar spring; $F_{ur,\theta}$ is

the temperature-dependent ultimate strength of the concrete containing rebar spring; $d_{yr,\theta}$ is the spring deformation when the rebar stress reaches the yield stress; $d_{ur,\theta}$ is the spring deformation when the rebar stress reaches the ultimate strength; A_r is the overall area of the rebars. When the spring force exceeds $F_{ur,\theta}$, an arbitrary small stiffness of 10 N/mm is given to the spring to simulate the rebars pull-out phenomenon, while avoiding numerical singularity. The stiffness of the rebar spring under tension K_{RC} can be calculated as:

$$K_{RC} = \begin{cases} F_{yr,\theta}/d_{yr,\theta} & (F_{RC} \leq F_{yr,\theta}) \\ (F_{ur,\theta} - F_{yr,\theta})/(d_{ur,\theta} - d_{yr,\theta}) & (F_{yr,\theta} < F_{RC} \leq F_{ur,\theta}) \\ 10 & (F_{RC} > F_{ur,\theta}) \end{cases} \quad (9)$$

in which F_{RC} is the tension force of the rebar spring.

1.2 Beam bottom flange in contact with column

When the end of the composite beam has rotated to the point that the beam bottom flange contacts the column, the spring representing the beam bottom flange in contact with column is activated. On the basis of Quan's research [34], a further simplified trilinear model is proposed in this research to represent the force-deformation behaviour of such a spring, as shown in Figure 4. In the figure, $F_{\rho,b\theta}$ and $F_{y,b\theta}$ are the temperature-dependent forces when the stress within the lower half I section of the beam reaches the proportional limit and yield stress, respectively. $F_{\rho,b\theta}$ and $F_{y,b\theta}$ can be calculated according to Eqns.(10) and (11), respectively. In these equations, $f_{\rho,\theta}$ and $f_{y,\theta}$ are the temperature-dependent proportional limit stress and the yield stress of the beam, respectively. t_f is the beam bottom flange thickness; b_f is the beam bottom flange width; t_w is the beam web thickness, and $E_{b,\theta}$ is the temperature-dependent beam Young's Modulus. It has been concluded by Quan et al. [34] that it is reasonable to assume that the buckling length of the beam bottom flange is equal to the height of the steel beam d . Therefore, $d_{\rho,b\theta}$ can be

calculated according to Eq.(12). $d_{y,b\theta}$ is equal to $0.02d$, which means that $d_{y,b\theta}$ is the deformation when the strain of the lower half of the beam reaches 0.02.

$$F_{\rho,b\theta} = f_{\rho,\theta}(t_f b_f + (d - 2t_f)t_w/2) \quad (10)$$

$$F_{y,b\theta} = f_{y,\theta}(t_f b_f + (d - 2t_f)t_w/2) \quad (11)$$

$$d_{\rho,b\theta} = F_{\rho,b\theta}d/E_{b,\theta}(t_f b_f + (d - 2t_f)t_w/2) \quad (12)$$

According to Quan et al. [34], the bottom flange buckling of the beam usually occurs when the force in the beam bottom flange falls between $F_{\rho,b\theta}$ and $F_{y,b\theta}$. After the spring force exceeds $F_{y,b\theta}$, an arbitrary small stiffness of 10 N/mm is given to the spring to simulate the post buckling behaviour, as well as to avoid numerical divergence problems.

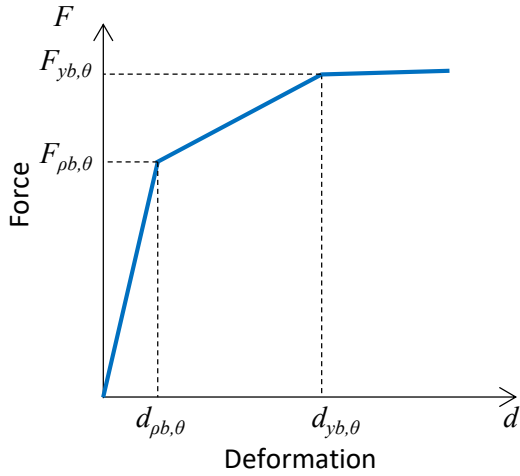


Figure 4. Force-deformation relationship of the spring representing beam bottom flange in contact with column

The stiffness of the beam bottom flange in contact with column spring K_{BC} can be calculated as:

$$K_{BC} = \begin{cases} F_{\rho,b\theta}/d_{\rho,b\theta} & (F_{BC} \leq F_{\rho,b\theta}) \\ (F_{y,b\theta} - F_{\rho,b\theta})/(d_{y,b\theta} - d_{\rho,b\theta}) & (F_{\rho,b\theta} < F_{BC} \leq F_{y,b\theta}) \\ 10 & (F_{BC} > F_{y,b\theta}) \end{cases} \quad (13)$$

in which F_{BC} is the reaction of the beam bottom flange in contact with the column.

1.3 Fin-plate connection bolt row

1.3.1 Plate in bearing

The spring type representing the plate in bearing covers the bearing deformation of the bolt hole of one plate due to its contact with the bolt shank. In a fin-plate connection, where the fin-plate and the beam web are bolted together, the deformation of the hole of either the fin-plate or the beam web is represented by one spring. Therefore, two plate-in-bearing springs exist within one bolt row, representing the deformations of the bolt holes of the fin-plate and the beam web, respectively. The relationship (Eq. (14)) between the deformation Δ_b of the plate in bearing and the bearing force F_b , developed by Sarraj et al. [35], is adopted in this research.

$$\frac{F_b}{F_{b,Rd}} = \frac{\psi \bar{\Delta}}{(1 + \bar{\Delta}^{0.5})^2} - \phi \bar{\Delta} \quad (14)$$

where,

$$\bar{\Delta} = \Delta_b K_i / F_{b,Rd} \quad (15)$$

in which K_i is the plate bearing stiffness, and $F_{b,Rd}$ is the plate bearing resistance. Plate in bearing is influenced by three primary factors: plate bearing at the hole with stiffness K_{br} , plate bending with stiffness K_b and plate shearing with stiffness K_v . Therefore, K_i can be calculated using Eq. (16).

$$K_i = \frac{1}{\frac{1}{K_{br}} + \frac{1}{K_b} + \frac{1}{K_v}} \quad (16)$$

where,

$$K_{br} = \Omega t f_y \left(\frac{d_b}{25.4} \right)^{0.8} \quad (17)$$

$$K_b = 32Et \left(\frac{e_2}{d_b} - 0.5 \right)^3 \quad (18)$$

$$K_v = 6.67Gt \left(\frac{e_2}{d_b} - 0.5 \right) \quad (19)$$

in which t is the plate thickness; f_y is the yield stress of the plate; E is the Young's Modulus of the plate; and G is the Shear Modulus of the plate.

The coefficients ψ , Φ and Ω are obtained by curve-fitting to the FE results by Sarraj et al. [35]. These three parameters vary with temperature, bolt diameter d_b and the ratio between plate end distance e_2 and d_b . Their values under different temperatures and end distances are listed in the Appendix, Table A.1. It is worth noting that for the particular case when the connection has a small end distance ($e_2 < 2d_b$) and is in tension at ambient temperature, it has been decided to use the values of ψ and Φ proposed by Richard and Abbott [36] in this research, as they result in better results. Moreover, Sarraj et al. [35] obtained the values of ψ , Φ and Ω based on FE models of connections using only M20 and M24 bolts. In this study, the values of ψ , Φ and Ω for connections of M20 bolts are used for cases of bolt diameter less or equal to 20mm, and those developed for connections of M24 bolts are used for cases of bolt diameter larger than 20mm.

According to Sarraj's findings, when the plate is in tension, the plate bearing resistance $F_{b,Rd}$ can be calculated using Eq. (20). e_2/d_b is set to be 3 when it is larger than 3. When the plate is in compression, $F_{b,Rd}$ calculated by Eq. (20) should be reduced, using a reduction factor of 0.92.

$$F_{b,Rd} = \frac{e_2}{d_b} \times f_u d_b t \quad (20)$$

Reduction factors are applied to the high-temperature yield strength f_y , ultimate strength f_u and elastic modulus E of the plate. The reduction factors could be based on test data or given by design guidance. The curved force-deformation relationship proposed by Sarraj [19] has been simplified into a quadrilinear relationship with the vertical coordinates of the inflection points to be $0.5F_{b,Rd}$, $0.75F_{b,Rd}$, $0.9F_{b,Rd}$ and $F_{b,Rd}$. The corresponding horizontal coordinates are the Δ_b calculated according to Eqns. (14) and (15). It is assumed that the plate-in-bearing spring fractures at a deformation that is equal to the bolt diameter d_b when under tension. This is defined by comparing the FE result and Yu's test [22] in Section 2.1. The plate bearing spring does not fracture when under compression. In order to avoid numerical singularity, an arbitrary small stiffness of 10 N/mm is given to the spring between the deformation $\Delta_{b,Rd}$, corresponding to the plate ultimate strength, and the deformation that equals to the bolt diameter d_b . The indicative force-deformation curve of the plate in bearing spring is shown in Figure 5.

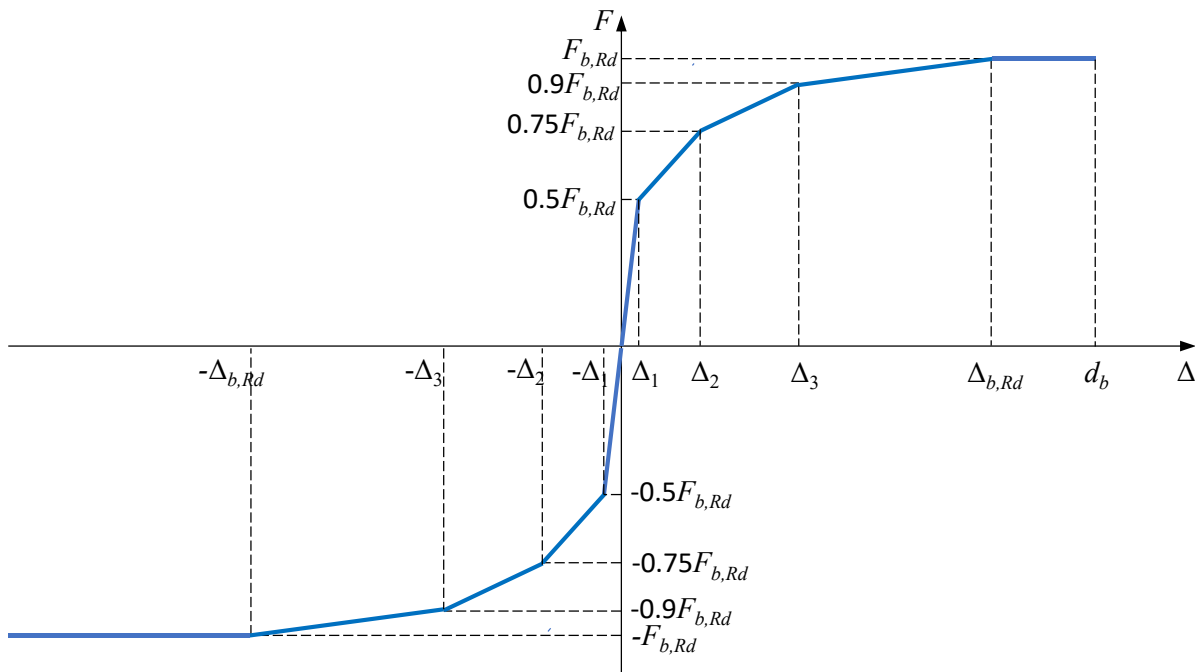


Figure 5. Indicative force-deformation curve of the plate in bearing spring

The stiffness of the plate-in-bearing spring K_{PB} can be calculated as:

$$K_{PB} = \begin{cases} 0.5F_{b,Rd}/\Delta_1 & (F_{PB} \leq 0.5F_{b,Rd}) \\ (0.75F_{b,Rd} - 0.5F_{b,Rd})/(\Delta_2 - \Delta_1) & (0.5F_{b,Rd} < F_{PB} \leq 0.75F_{b,Rd}) \\ (0.9F_{b,Rd} - 0.75F_{b,Rd})/(\Delta_3 - \Delta_2) & (0.75F_{b,Rd} < F_{PB} \leq 0.9F_{b,Rd}) \\ (F_{b,Rd} - 0.9F_{b,Rd})/(\Delta_{b,Rd} - \Delta_3) & (0.9F_{b,Rd} < F_{PB} \leq F_{b,Rd}) \\ 10 & (F_{b,Rd} < F_{PB} \text{ \& } \Delta_{PB} \leq d_b) \\ 0 & (\Delta_{PB} > d_b) \end{cases} \quad (21)$$

in which F_{PB} is the force of the plate-in-bearing spring; Δ_{PB} is the deformation of this spring.

1.3.2 Bolt in shear

The relationship between the bolt shear deformation Δ_s and the shear force F_s (calculated by Eq. (22)) used in this research was developed by Sarraj [35], which curve-fits the FE analysis results to a modified Ramberg-Osgood expression [37].

$$\Delta_s = \frac{F_s}{K_{v,b}} + \Omega_s \left(\frac{F_s}{F_{v,Rd}} \right)^6 \quad (22)$$

where,

$$F_{v,Rd} = 0.6f_{ub}A_s \quad (23)$$

$$K_{v,b} = \frac{0.15GA_s}{d_b} \quad (24)$$

In Eq. (22), Δ_s is the bolt shear deformation; F_s is the applied bolt shear force. $K_{v,b}$ is the bolt shear stiffness; G is the Shear Modulus of the plate; A_s is the stressed area of bolt, and $F_{v,Rd}$ is the bolt ultimate shear resistance. The value Ω_s , which was obtained from the curve-fitting procedure, is listed in the Appendix Table A.1. The force-deformation relationship is simplified into a quadrilinear line with the vertical coordinates of the inflection points to be $0.5F_{v,Rd}$, $0.75F_{v,Rd}$, $0.9F_{v,Rd}$ and $F_{v,Rd}$. The corresponding

horizontal coordinates Δ_s can be calculated according to Eqns. (22) - (24). It is assumed that the bolt-in-shear spring fractures at a deformation of a quarter of the bolt diameter ($0.25d_b$). This is defined according to the observation of Yu's test [22] and comparing the FE result and Yu's test [22] in Section 2.1. In order to avoid numerical singularity, an arbitrary small stiffness of 10 N/mm is given to the spring between the plate deformation of $\Delta_{v,Rd}$ and $0.5d_b$. The indicative force-deformation curve of the bolt in shear spring is shown in Figure 6. At high temperatures, f_{ub} and G are multiplied by the reduction factors to represent the degradation of material. The reduction factors could be based on test data or given by design guidance.

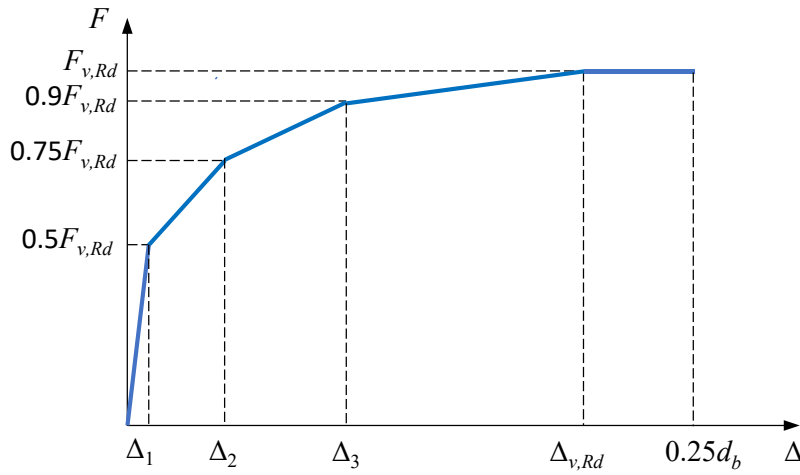


Figure 6. Indicative force-deformation curve of the bolt in shear spring

The stiffness of the bolt-in-shear spring K_{BS} can be calculated as:

$$K_{BS} = \begin{cases} 0.5F_{v,Rd}/\Delta_1 & (F_{BS} \leq 0.5F_{v,Rd}) \\ (0.75F_{v,Rd} - 0.5F_{v,Rd})/(\Delta_2 - \Delta_1) & (0.5F_{v,Rd} < F_{BS} \leq 0.75F_{v,Rd}) \\ (0.9F_{v,Rd} - 0.75F_{v,Rd})/(\Delta_3 - \Delta_2) & (0.75F_{v,Rd} < F_{BS} \leq 0.9F_{v,Rd}) \\ (F_{v,Rd} - 0.9F_{v,Rd})/(\Delta_{v,Rd} - \Delta_3) & (0.9F_{v,Rd} < F_{BS} \leq F_{v,Rd}) \\ 10 & (F_{v,Rd} < F_{BS} \text{ \& } \Delta_{BS} \leq 0.25d_b) \\ 0 & (\Delta_{BS} > 0.25d_b) \end{cases} \quad (25)$$

in which F_{BS} is the force of the bolt-in-shear spring; Δ_{BS} is the deformation of this spring.

1.3.3 Bolt friction

Taib [23] proposed a friction model with the maximum friction force calculated according to Eq.(26), where R_f is the maximum friction force; μ is the slip factor; f_{ub} is the tensile resistance of a single bolt, and A_s is the stressed area of bolt. BS EN 1090-2 [38] gives the values of μ within a range of 0.2 to 0.5, depending on the class of friction surfaces. The value of 0.2 is adopted in this research to provide a conservative solution.

$$R_f = 0.28\mu f_{ub} A_s \quad (26)$$

In Taib's model [23], the maximum friction force is reached when the bolt friction displacement reaches 0.1 of the bolt hole clearance (d_c), which is the gap between the bolt hole edge and the bolt shank to allow installation error. After that, the friction force persists as a plateau until the bolt makes positive contact with the bolt hole edge. The bolt post-contact friction decreases gradually with movement. In this research, Taib's model has been simplified. It is assumed that the friction increases linearly until the bolt contacts the bolt hole edge. This is to avoid possible numerical singularity between $0.1d_c$ and d_c . When the maximum friction force is reached, the plateau is kept even after when the bolt contact with the edge. The simplified model can still reasonably reflect the static friction after the bolt of a connection contacts the edge. An illustrative graph of Taib's friction model [23] and the simplified friction model in this research are shown in Figure 7. Reduction factors should be applied to f_{ub} at elevated temperatures.

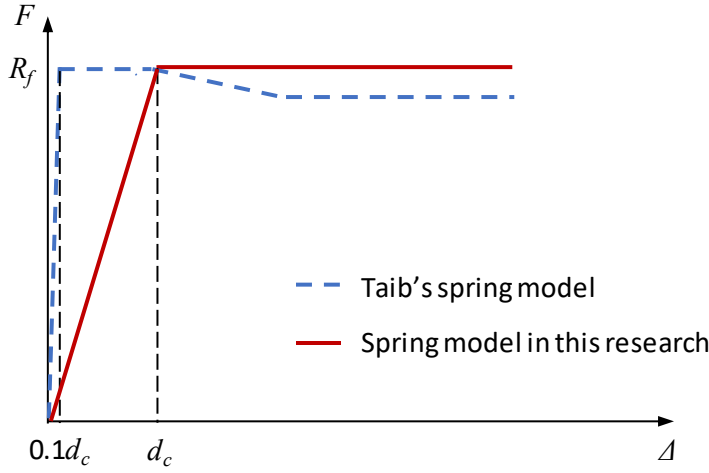


Figure 7. Force-deformation curves of the friction spring

The stiffness of the bolt-friction spring K_{BF} can be calculated as:

$$K_{BF} = \begin{cases} R_f/d_c & (F_{BF} \leq R_f) \\ 10 & (F_{BF} > R_f) \end{cases} \quad (27)$$

in which F_{BF} is the force of the bolt-friction spring.

The stiffness of each bolt row spring is given by:

$$K_{BR} = \frac{1}{\frac{1}{K_{PB1}} + \frac{1}{K_{PB1}} + \frac{1}{K_{BS}}} + K_{BF} \quad (28)$$

1.4 Formulation of the connection element

In order to include the component-based composite fin-plate connection element in Vulcan, the usual calculation principle should be followed to derive the behaviour of the connection element.

$$\mathbf{F} = \mathbf{K}\mathbf{u} \quad (29)$$

in which \mathbf{F} is the vector of elemental applied forces, \mathbf{K} is the elemental stiffness matrix of the component-based composite fin-plate connection element, and \mathbf{u} is the vector of elemental displacements.

Due to the nonlinear behaviour of the proposed connection element, Eq. (29) is solved iteratively using the

elemental tangent stiffness matrix \mathbf{K}' , incremental applied forces $\Delta \mathbf{F}$ and elemental displacements $\Delta \mathbf{u}$.

Therefore, for each incremental step, Eq. (29) can be expressed as:

$$\Delta \mathbf{F} = \mathbf{K}' \Delta \mathbf{u} \quad (30)$$

with

$$\Delta \mathbf{F}^T = [\Delta N_{x,i} \Delta V_{y,i} \Delta V_{z,i} \Delta M_{x,i} \Delta M_{y,i} \Delta M_{z,i} \Delta N_{x,j} \Delta V_{y,j} \Delta V_{z,j} \Delta M_{x,j} \Delta M_{y,j} \Delta M_{z,j}] \quad (31)$$

and

$$\Delta \mathbf{u}^T = [\Delta u_i \Delta v_i \Delta w_i \Delta \theta_{x,i} \Delta \theta_{y,i} \Delta \theta_{z,i} \Delta u_j \Delta v_j \Delta w_j \Delta \theta_{x,j} \Delta \theta_{y,j} \Delta \theta_{z,j}] \quad (32)$$

The elemental tangent stiffness matrix \mathbf{K}' can be expressed as:

$$\mathbf{K}' = \begin{bmatrix} k_{1,1} & 0 & 0 & 0 & k_{1,5} & 0 & k_{1,7} & 0 & 0 & 0 & k_{1,11} & 0 \\ 0 & k_{2,2} & 0 & 0 & 0 & 0 & 0 & k_{2,8} & 0 & 0 & 0 & 0 \\ 0 & 0 & k_{3,3} & 0 & 0 & 0 & 0 & 0 & k_{3,9} & 0 & 0 & 0 \\ 0 & 0 & 0 & k_{4,4} & 0 & 0 & 0 & 0 & 0 & k_{4,10} & 0 & 0 \\ k_{5,1} & 0 & 0 & 0 & k_{5,5} & 0 & k_{5,7} & 0 & 0 & 0 & k_{5,11} & 0 \\ 0 & 0 & 0 & 0 & 0 & k_{6,6} & 0 & 0 & 0 & 0 & 0 & k_{6,12} \\ k_{7,1} & 0 & 0 & 0 & k_{7,5} & 0 & k_{7,7} & 0 & 0 & 0 & k_{7,11} & 0 \\ 0 & k_{8,2} & 0 & 0 & 0 & 0 & 0 & k_{8,8} & 0 & 0 & 0 & 0 \\ 0 & 0 & k_{9,3} & 0 & 0 & 0 & 0 & 0 & k_{9,9} & 0 & 0 & 0 \\ 0 & 0 & 0 & k_{10,4} & 0 & 0 & 0 & 0 & 0 & k_{10,10} & 0 & 0 \\ k_{11,1} & 0 & 0 & 0 & k_{11,5} & 0 & k_{11,7} & 0 & 0 & 0 & k_{11,11} & 0 \\ 0 & 0 & 0 & 0 & 0 & k_{12,6} & 0 & 0 & 0 & 0 & 0 & k_{12,12} \end{bmatrix} \quad (33)$$

in which

$$k_{1,1} = k_{7,7} = -k_{1,7} = -k_{7,1} \sum_{i=1}^n k_{T,i} + \sum_{i=1}^n k_{C,i} \quad (34)$$

$$\begin{aligned}
k_{1,5} &= k_{5,1} = k_{7,11} = k_{11,7} = -k_{1,11} = -k_{11,1} = -k_{5,7} = -k_{7,5} \\
&= \sum_{i=1}^n h_{T,i} k_{T,i} + \sum_{i=1}^n h_{C,i} k_{C,i}
\end{aligned} \tag{35}$$

$$k_{5,5} = k_{11,11} = -k_{5,11} = -k_{11,5} = \sum_{i=1}^n h_{T,i}^2 k_{T,i} + \sum_{i=1}^n h_{C,i}^2 k_{C,i} \tag{36}$$

$$k_{2,2} = k_{3,3} = k_{4,4} = k_{6,6} = k_{8,8} = k_{9,9} = k_{10,10} = k_{12,12} = 10^{20} \tag{37}$$

$$k_{2,8} = k_{8,2} = k_{4,10} = k_{10,4} = k_{6,12} = k_{12,6} = k_{3,9} = k_{9,3} = -10^{20} \tag{38}$$

in which $k_{T,i}$ is the tensile stiffness of the i^{th} spring; $k_{C,i}$ is the compressive stiffness of the i^{th} spring; It is worth noting that, when the i^{th} spring is in tension, $k_{T,i}$ takes effect, and $k_{C,i}$ is zero, and vice versa when this spring is in compression. $h_{T,i}$ is the lever arm of the i^{th} spring when it is in tension, and $h_{C,i}$ is its lever arm in compression. The lever arm is measured from the axis of the spring to the reference axis of the composite connection element, which is located at the mid-surface of the rebar layer within the concrete slab. n is the total number of the springs. In Eqns. (37) and (38), 10^{20} and -10^{20} represent infinite and zero stiffness, respectively. The governing Eq. (30), together with the stiffness matrix Eq. (33), forms the backbone of the connection element.

2 Validating the component-based model against tests

The proposed component-based composite fin-plate connection model has been implemented into the software Vulcan. In this section, the component-based model will be validated against a range of existing tests at ambient, constant high temperatures and increasing elevated temperatures. Due to the lack of

experimental data on the connection bolt row forces in a composite beam, the component-based model was firstly validated against Yu's tests [22] on bare steel fin-plate connections. This is to verify the setup of the connection bolt row springs and the spring representing the beam bottom flange in contact with the column within a composite fin-plate connection, by deactivating the concrete flange containing the rebar spring. Subsequently, the component-based composite fin-plate connection was validated against NIST composite beam tests [28, 29], to verify the concrete flange containing the rebar spring and the overall performance of the whole composite fin-plate connection model.

2.1 Validation against Yu's tests

Yu et al. [22] carried out a series of tests on bare steel fin-plate connections subjected to combinations of tension force and shear force at ambient temperature and constant high temperatures. The connections were also subjected to moment produced by eccentricity of the tension force and the shear force. The validations were carried out for connections with three rows of Grade 8.8 M20 bolts, tested at 20°C, 450°C, 550°C and 650°C.

2.1.1 The tested connections and Vulcan model

The tested specimens were composed of a UC254×89 column section, a UB 305×165×40 beam section and a three-bolt-row fin-plate connection which connected the column section to the beam section. The fin-plate was 200mm × 8mm (depth × thickness). Inclined load was applied to the end of the UB 305×165×40 beam. The specimens were loaded with two initial angles (α) of 35 degrees and 55 degrees to achieve different combination of shear force and tensile force applied to the specimens. The detailed dimensions of the tested specimens are shown in Figure 8.

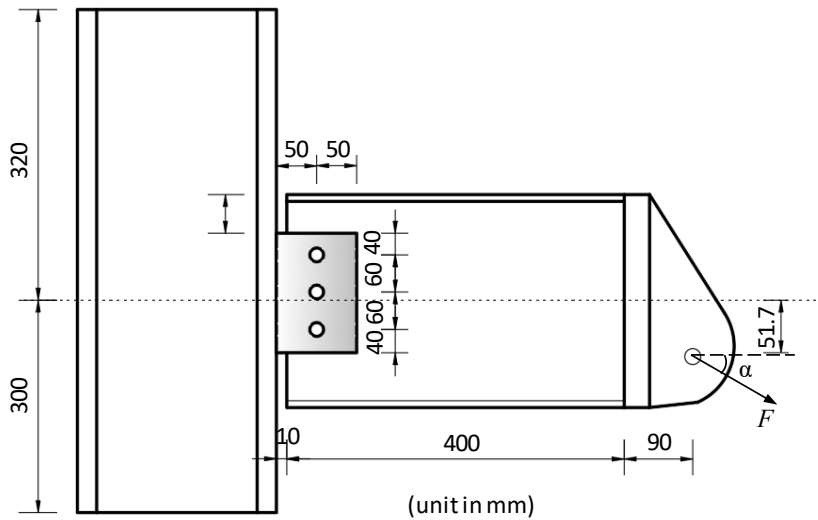


Figure 8. Detailed dimensions of the tested specimens

The FE software Vulcan was used to model the fin-plate connections in Yu's tests. It is worth noting that, in Vulcan, a finer mesh does not necessarily lead to more accurate simulation results. The recommended element sizes for connection elements, beam element and slab element are 1mm, 1000mm, and 1000 mm X 1000mm (length X width), respectively [39]. The connection element was modelled using the proposed two-node composite fin-plate connection element with a length of 1mm. The concrete flange containing the rebar spring was deactivated. The connected 490mm steel beam was modelled using one three-node beam element. The Vulcan model of Yu's connection is shown in Figure 9. Axial forces along the X axis, the Z axis and the moment about the Y axis were applied to Node 4 first, and the load was kept constant while the model was heated.

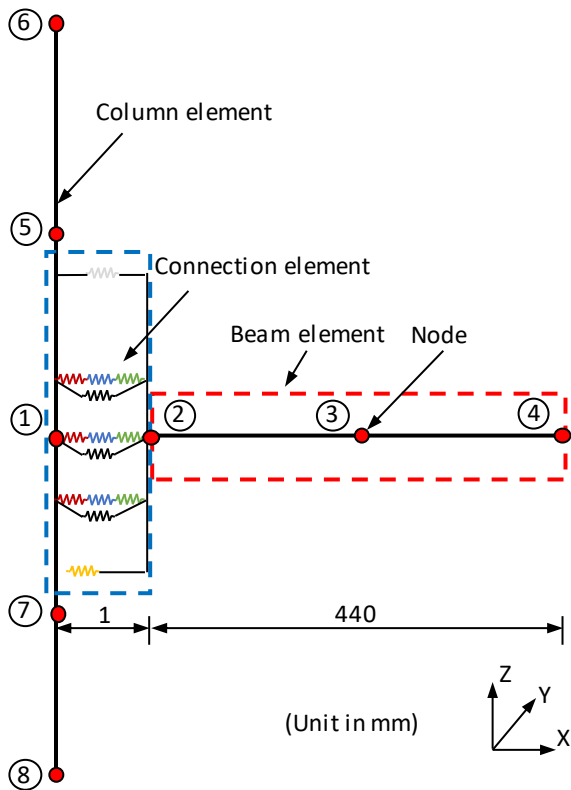


Figure 9. Outline of the Vulcan model of Yu's connection

In Yu's tests, the steel columns were made of S355 steel; the fin-plates and the steel beams were made of S275 steel, and the bolts were made of A36 steel. As the fin-plate was made of the same material with the beam web, but was 2mm thicker than the beam web, the beam material properties played the dominant role when the failure mode was plate fracture. In the Vulcan models, the material properties of S275 (for beams and fin-plates) and the tensile strength of the bolts at ambient temperature tested by Yu [22] were used. For S275, the measured yield strength is 356MPa, the ultimate strength is 502MPa, and the elastic modulus is 1.76×10^5 MPa. The ultimate strength of the bolts is 713MPa. As Yu did not measure the material properties at high temperatures, in the Vulcan modelling the reduction factors of the steel were obtained from different research sources, which reported the reduction factors of S275 and A36 steels separately. The reduction factors of the S275 yield strength and ultimate strength at high temperatures were chosen from

Renner's tests [40]. The reduction factors of the bolt ultimate strength at high temperatures in Hu's tests [41] were used in the modelling. Hu et al. [41] did not record the reduction factor at 700°C; therefore, the Eurocode 3 [4] recommended reduction factor of 0.1 was used for the bolts at 700°C. The Eurocode 3 [4] recommendation was used for the Elastic Modulus of the bolts. The reduction factors for different materials are listed in Table 1.

Table 1. Reduction factors (RF) of the materials

		Temperature (°C)	20	100	200	300	400	500	600	700	800
Beam section and fin-plate	Yield strength RF	1.00	-	-	-	0.91	0.62	0.31	0.14	-	-
	Tensile strength RF	1.00	-	-	-	0.87	0.47	0.23	0.11	-	-
	Elastic modulus RF	1.00	1.00	0.90	0.80	0.70	0.60	0.31	0.13	0.09	0.09
	Shear strength RF	1.00	1.00	1.00	1.00	0.71	0.39	0.20	-	-	-
Bolts		Elastic modulus RF	1.00	1.00	0.90	0.80	0.70	0.60	0.31	0.13	0.09

2.1.2 Results and discussions

The force-deformation comparisons between the results of Yu's tests and those of the Vulcan modelling are shown in Figure 10 and Figure 11 for the initial loading angles of 35° and 55°, respectively. During the simulation, the bolt hole clearance was defined as between 1.5mm and 4mm so that the initial slippage phase of the force-rotation curves fit the test results. The ultimate strengths of different springs are listed in Table 2, in which $F_{b,Rdbeam}$ and $F_{b,Rdplate}$ are the ultimate bearing strengths of beam web and the fin-plate, respectively. $F_{v,Rd}$ is the bolt shear strength; R_f is the friction force; $F_{r,CM}$ and $F_{r,Test}$ are the connection ultimate strength calculated from the component-based model and obtained from the tests, respectively. It can be

seen that the Vulcan FE results compare reasonably well with the test results.

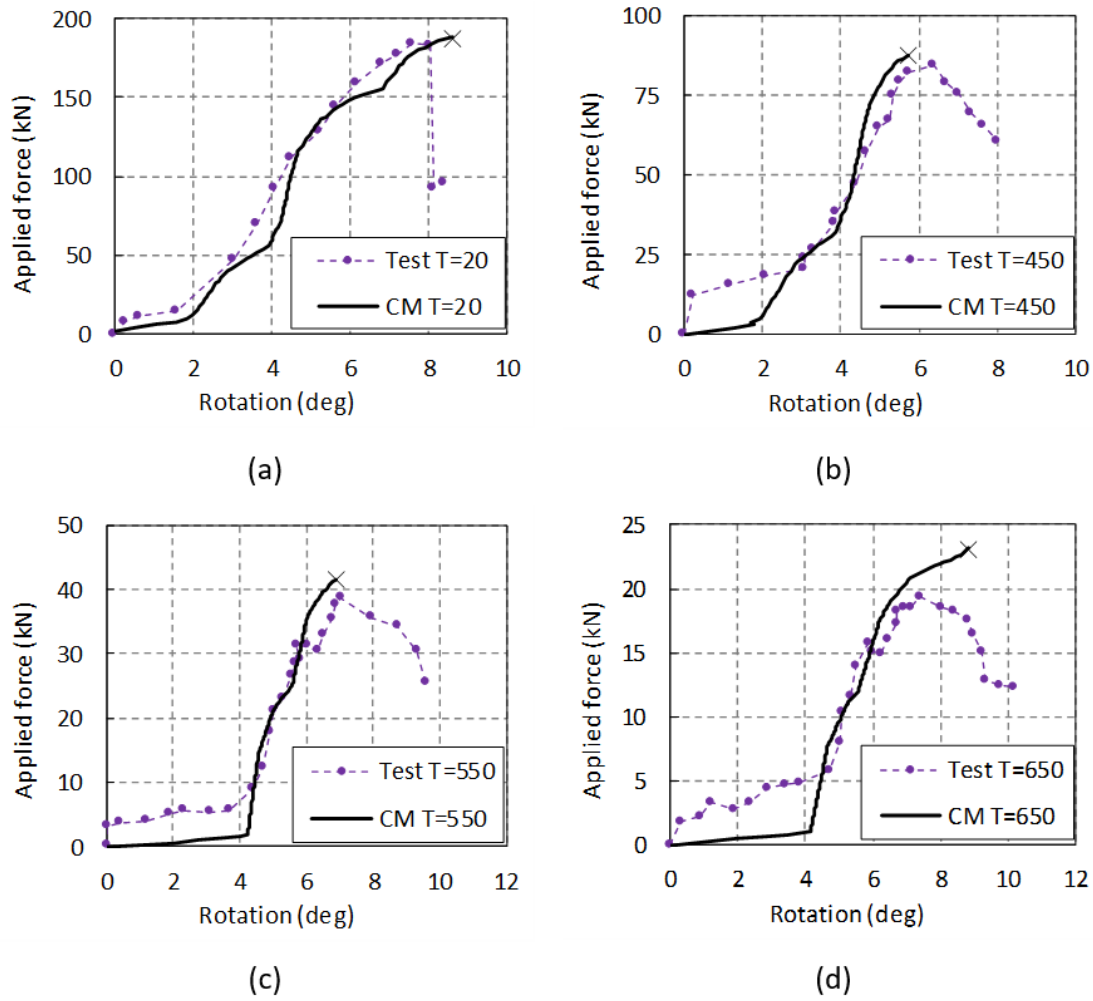


Figure 10. Force-deformation comparisons between Yu's tests and Vulcan modelling with initial angle (α) of 35 degrees: (a) $T=20^{\circ}\text{C}$, (b) $T=450^{\circ}\text{C}$, (c) $T=550^{\circ}\text{C}$, and (d) $T=650^{\circ}\text{C}$

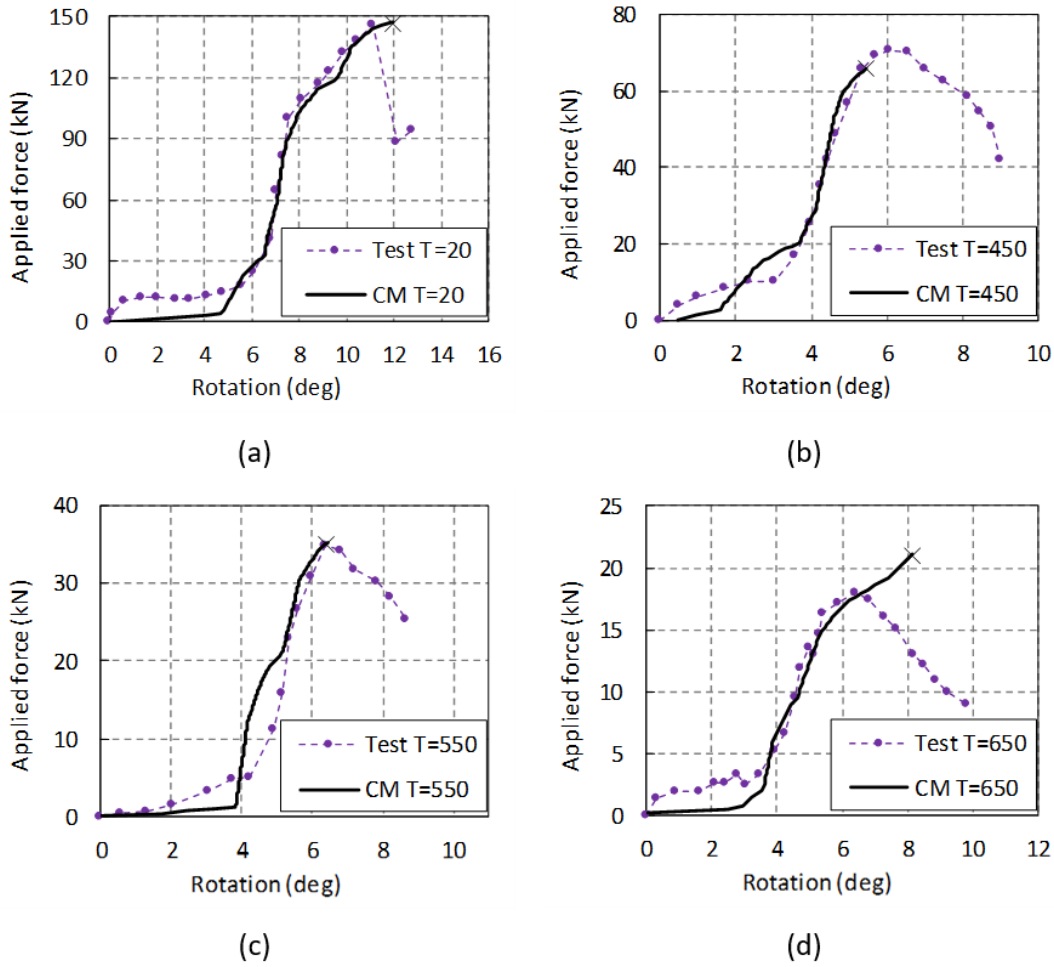


Figure 11. Force-deformation comparisons between Yu's tests and Vulcan modelling with initial angle (α) of 55 degrees: (a) $T=20^{\circ}\text{C}$, (b) $T=450^{\circ}\text{C}$, (c) $T=550^{\circ}\text{C}$, and (d) $T=650^{\circ}\text{C}$

Table 2. Comparisons of the connection strengths

Loading angle (degrees)	Temperature	$F_{b,Rdbeam}$	$F_{b,Rdplate}$	$F_{v,Rd}$	R_f	$F_{r,CM}$	$F_{r,Test}$	$F_{r,CM}/F_{r,Test}$
	($^{\circ}\text{C}$)	(kN)	(kN)	(kN)	(kN)	(kN)	(kN)	
	20	200.80	120.48	129.99	12.13	188.00	172.51	1.09
35	450	134.54	80.72	71.50	5.95	87.71	84.33	1.04
	550	70.28	42.17	38.35	3.52	41.50	35.61	1.16

55	650	34.14	20.48	19.50	1.82	23.19	19.91	1.16
	20	200.8	120.48	129.99	12.13	147.00	145.92	1.01
	450	134.54	80.72	71.50	5.95	66.00	70.80	0.93
	550	70.28	42.17	38.35	3.52	35.00	34.82	1.01
	650	34.14	20.48	19.50	1.82	21.09	17.98	1.17

During the analysis, it was observed that the spring ductility significantly relied on the plate deformation rather than the bolt in shear deformation. When the ultimate shear strength of the bolt was significantly lower than that of the plate in bearing, the bolt failed without allowing the plates to develop much deformation. In such cases, when the first bolt row failed due to tension, the bottom bolt row normally would not contact the bolt hole edge due to a lack of connection rotation. No further connection stiffness increase was observed on the force-rotation curves. This situation applies to all the connections under temperatures of 450°C and 550°C shown in Figure 10 and Figure 11. When the difference between the ultimate bolt shear strength and plate in bearing strength was small, or when the plate was the weakest part of the connection, the plate deformation could be sufficiently developed. Therefore, when the top bolt row failed in tension, the bottom bolt row could make contact with the bolt hole edge, and the connection redeveloped its stiffness. This situation applies to the connections at 650°C, as shown in Figures 10 and 11. It can be seen that the FE results for the connection resistance at 650°C were higher than those in the tests. This may be because that the reduction factors used for the bolts and/or the plates at 650°C were not sufficiently precise and that the strength difference between the bolts and the plates was larger than in reality.

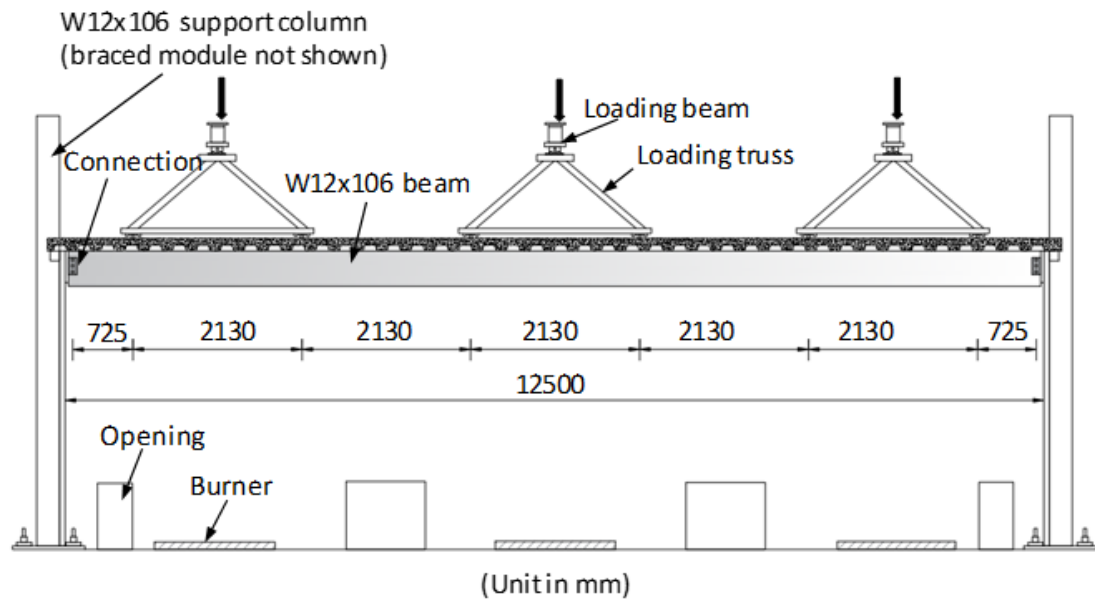
2.2 Validation against NIST composite beam tests

NIST carried out five tests on long-span composite beams at elevated temperatures [28, 29]. In one of the

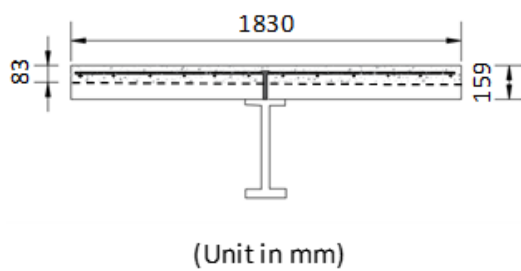
five tests with the specimen name of CB-SP-SC, fin-plate connections were installed at the beam ends. Slab continuity was achieved by connecting the rebars and welded fabrics in the concrete slab to the braced columns. In this section, this test is used to validate the composite fin-plate connection in Vulcan.

2.2.1 Test setup

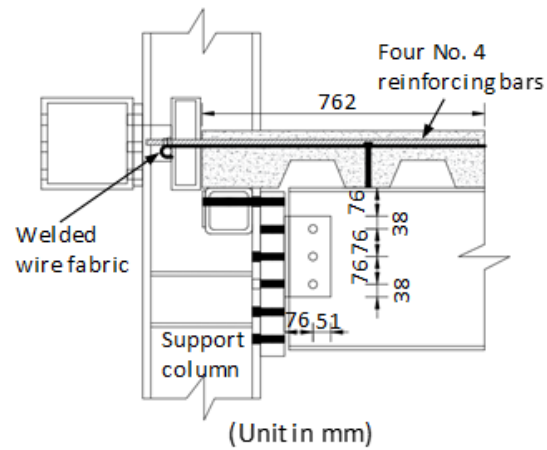
The test set-up and the detailed specimen dimensions are shown in Figures 12 (a) and 12 (b). The tested composite beam consisted of a lightweight concrete slab on 20-gauge galvanized 76mm deep ribbed steel decking. The thickness of the concrete above the ribs was 83 mm. The slab width was 1.83 m. The steel beam underneath the concrete slab was W18 × 35, connected to W12 × 106 columns. The centre-to-centre distance between the bolt lines on the beam web was 12.2m. 3.4mm-diameter plain steel wires in 150mm grids was placed at the mid-height of the topping. Four No. 4 reinforcing bars were distributed along the slab width at 457mm spacing, and were extended into the concrete by 762mm in length. The composite beam was supported by braced columns on both sides of the tested composite beam. All the steel wires and the reinforcing bars were linked to the braced columns to simulate the slab continuity. The measured lateral stiffness of the braced column was 180kN/mm. The beam was firstly loaded at six points with 17.67kN at each point, to represent an overall load of 106kN at ambient temperature, and then heated up with the load being constant.



(a)



(b)



(c)

Figure 12. Scale drawing of the NIST composite beam CB-SP-SC test [29]: (a) test set-up, (b) detailed dimensions of the tested beam, and (c) end support detail

The fin-plate connection was composed of three bolt rows connecting the plate and the beam web. The fin-plate thickness was 230mm × 127mm (depth × width) with a thickness of 11mm. The diameter of the bolts was 19mm. The end support details, including the connection dimensions are shown in Figure 12 (c).

2.2.2 Vulcan modelling

Member details, loading procedure and boundary conditions

The NIST composite beam test [28, 29] CB-SP-SC was modelled using Vulcan. In the model, the composite beam was connected to two columns at the ends of the composite beam. Outside the two columns, nine supporting springs were modelled at each end of the composite beam to simulate the effect of the braced columns. The two fin-plate connections at the ends of the composite beam were modelled using two-node connection elements with length 1mm. The beam was modelled with twelve three-node beam elements with the length of 1008mm. Each beam-end column was modelled with eight three-node beam elements with the length of 720mm. The slab was modelled using twenty-four nine-node slab elements with the element size of 1008 mm x 915mm (length x width). It was assumed that the slab and the steel beam were fully interactive. In order to model the braced columns, five additional supporting spring elements were attached to each side of the beam end to provide axial restraint to the beam's thermal expansion. The outline of the model is shown in Figure 13.

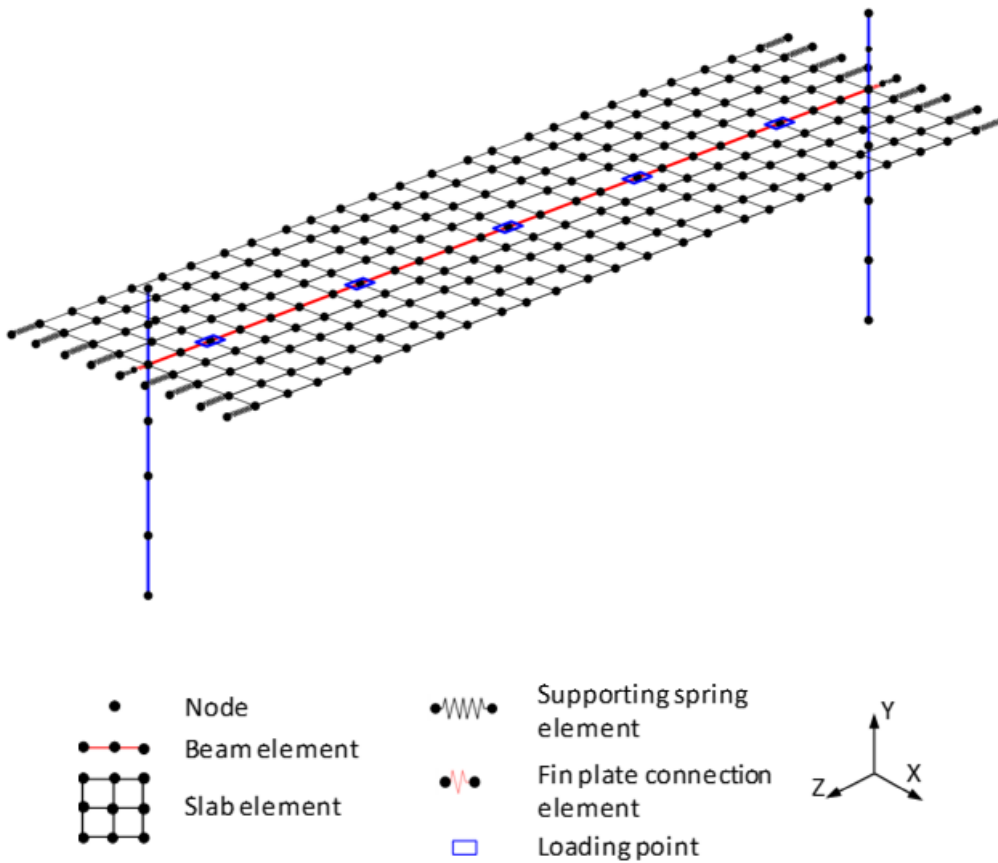


Figure 13. Outline of the Vulcan model of NIST composite beam test CB-SP-SC [28,29]

The nodes at the north and south edges of the slab were restrained from moving along the Y axis and from rotation about the Y and Z axes. The nodes on the east and west edges of the slab, except for those at the beam ends, were restrained from rotating across X and Y axis. The two nodes at the beam ends were restrained from rotating about the Z axis. The nodes on the outer side of the supporting spring elements were fixed. The stiffness of the ten supporting spring elements was 36 kN/mm to simulate the stiffness of the braced column with an overall stiffness of 180 kN/mm. Point loads of -17.667kN were applied to each loading point along the Y axis. As Vulcan cannot account for gravity load automatically, a uniformly distributed load of 0.00276N/mm² along the Y axis was applied to the slab elements to represent the gravity load of the concrete flange. Subsequently, the composite beam was heated while keeping the mechanical loads constant.

The temperatures of the composite beam were in accordance with the NIST experimental data [29], as shown in Figure 14. The temperature was assumed to be linearly distributed between the slab layers with measured temperatures. The steel decking was ignored when developing the FE model, as the contribution of the steel sheet to the resistance of the composite beam is negligible at high temperature.

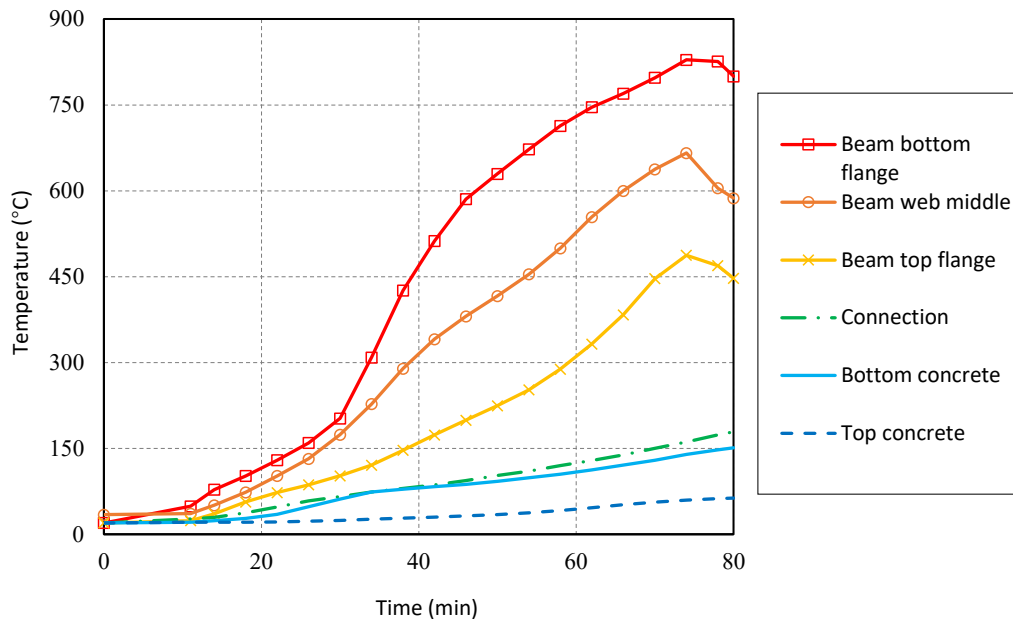


Figure 14. Temperature distribution along the composite beam cross-section from test data [29]

Material properties

In the Vulcan modelling, the material properties at ambient temperature were those measured from tests [28, 29], as shown in Table 3. The steel beam was made of A992 steel, the fin-plate was made of A36 steel, and the bolts were A325 steel.

Table 3. Material properties at ambient temperature

Components	ASTM	Yield strength	Tensile strength	Elastic
	designation	(MPa)	(MPa)	Modulus (MPa)

W18 x 35 Beam	A992	3.60E+02	4.70E+02	2.03E+05
Fin-plates	A36	3.48E+02	4.86E+02	2.06E+05
#4 Reinforcing bars	A615	4.69E+02	7.07E+02	1.90E+05
Welded wire fabric	A185	7.28E+02	7.57E+02	2.02E+05
Bolts	A325	9.02E+02	9.61E+02	2.06E+05

At elevated temperatures, the material reduction factors used in the Vulcan modelling were consistent with the data presented in Hu's tests [21], as shown in Table 4. For the reinforcing bars and the welded wire fabric, the reduction factors recommended by EC4 [33] were used in the modelling.

Table 4. Reduction factors (RF) of the materials

Component	Temperature (°C)	20	100	200	300	400	500	600	700	800
Beam section (W18 x 35)	Yield strength RF	1.00	1.00	1.00	1.00	1.00	0.78	0.47	0.23	0.11
	Tensile strength RF	1.00	0.95	0.98	1.02	0.90	0.66	0.40	0.20	0.10
	Elastic modulus RF	1.00	1.00	0.90	0.80	0.70	0.60	0.31	0.13	0.09
	Yield strength RF	1.00	0.97	0.97	0.96	0.89	0.78	0.52	0.28	0.17
Fin-plates	Tensile strength RF	1.00	0.96	1.11	1.09	0.95	0.65	0.36	0.19	0.10
	Elastic modulus RF	1.00	1.00	0.90	0.80	0.70	0.60	0.33	0.14	0.09
	Shear strength RF	1.00	1.00	1.00	1.00	0.62	0.36	0.20	0.10	0.10
Bolts	Elastic modulus RF	1.00	1.00	0.90	0.80	0.70	0.60	0.31	0.13	0.09

2.2.3 Results and discussions

The time-deflection comparison of the point that is 360mm from the beam mid-span between the results of

the test and that of Vulcan modelling is shown in Figure 15. The reason for comparing the deflection at this location is that this deflection has been measured in the NIST composite beam test [28, 29]. It can be seen that, before 35 minutes, the deflections of the test and Vulcan modelling are consistent. There is a discrepancy of deflection between 35 and 60 minutes when the beam bottom temperature is between approximately 450°C and 750°C. The maximum discrepancy of approximately 30% can be found at 55 minutes, when the bottom flange temperature is approximately 580°C.

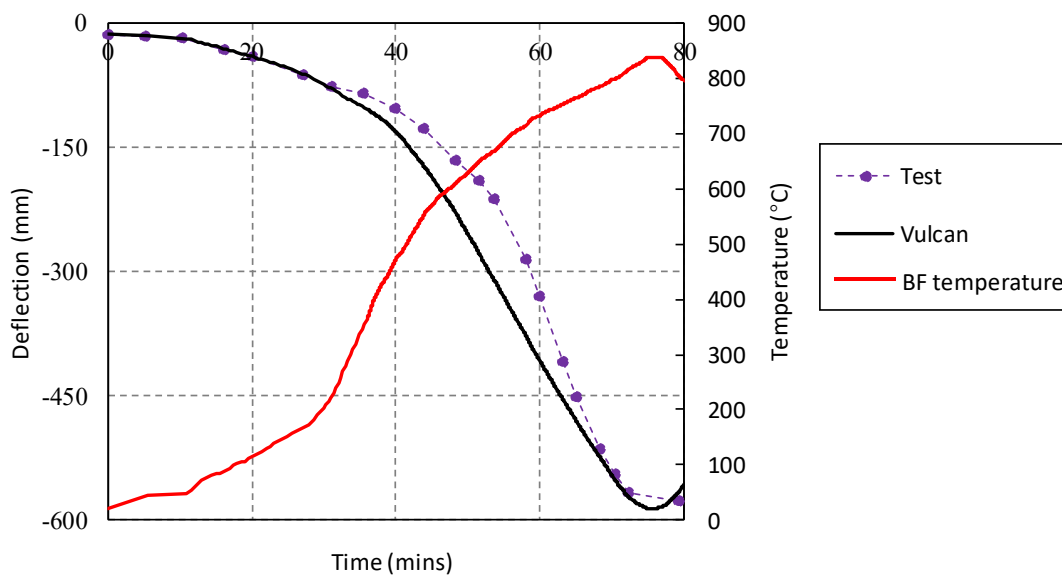


Figure 15. Time-deflection results comparison of the point close to the mid-span between the test and Vulcan modelling

The comparison of axial force versus the beam bottom flange temperature between the test and Vulcan modelling is shown in Figure 16. The axial force is the overall axial force of the nine supporting springs at one end of the beam. It is equivalent to the axial force applied to the braced columns in the test. Similar to the time-deflection comparison, when the bottom-flange temperature is between 450°C and 750°C, a relatively

large discrepancy can be found between the test and Vulcan modelling results, where the axial force from the Vulcan modelling is smaller than that in the test.

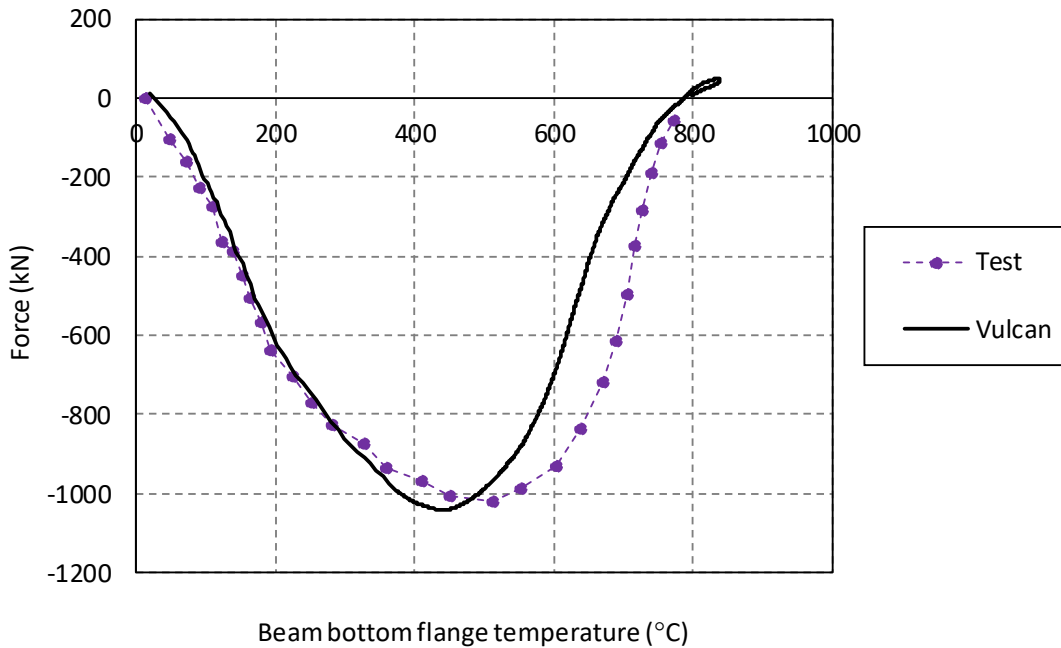


Figure 16. Force-beam bottom flange temperature results comparison between the test and Vulcan modelling

The possible reasons for the differences of the beam deflection and beam-end axial force between the Vulcan model and the test results could be that a reasonable assumption for the composite beam temperature, based on the temperature measured in the test, was made in the Vulcan model. The assumptions included that (1) temperatures were assumed to be uniformly distributed within the same layer of the composite slab, and (2) temperatures were assumed to be linearly distributed between the adjacent layers of the composite beam. The deflection and axial force discrepancies were especially noticeable at high temperature. Another reason could be that in the test the stiffness of the supporting column was 108kN/mm. Therefore, in the Vulcan modelling, the sum stiffness of the supporting springs at one beam side was 108kN/mm, whereas the

supporting force distribution along the slab east and west edges was unknown. As Vulcan only enables the user to define the boundary condition for each individual node, and the exact load distribution among these nodes were unknown, it is difficult to model the exact boundary condition of the composite beam. Therefore, it was assumed that the nodes on the east and west edges of the slab were supported by linear springs with equal stiffness of 36 kN/mm in the modelling that enables the overall axial restraint stiffness to be 108kN/mm. This assumption could not reflect the real axial restraint condition of the beam ends, due to the fact that the steel beam and the concrete flange had different thermal expansion coefficients. According to Yin and Wang's research [8, 9], the beam-end axial restraint condition has a significant influence on the beam deflection and axial force.

The rotations at the east and west beam-ends about the Y axis, according to the coordinate system in Figure 13, are compared in Figure 17. In this figure, the purple dashed line with markers represents the rotation about the Y axis at the beam west end from the test, and the orange dashed line with markers represents the rotation about the Y axis at the beam east end from the test. The corresponding solid lines represent the results from Vulcan modelling. It can be seen that, due to the high degree of nonlinearity of composite structures under high temperatures, the degradation of the concrete material itself and specimen imperfections, there was a reasonable discrepancy between the rotations at the east and west beam-ends from the test. The rotations obtained from the Vulcan model lie within a satisfactory range compared with the test results. It can be seen that the beam-end rotations increase up to an absolute value of 0.023 radians until 30 minutes from ignition, and then they remain at a constant value until approximately 55 minutes, when the absolute value of rotation decreases to 0.12 radians. The tendency of the rotation from Vulcan modelling is consistent with that of the test.

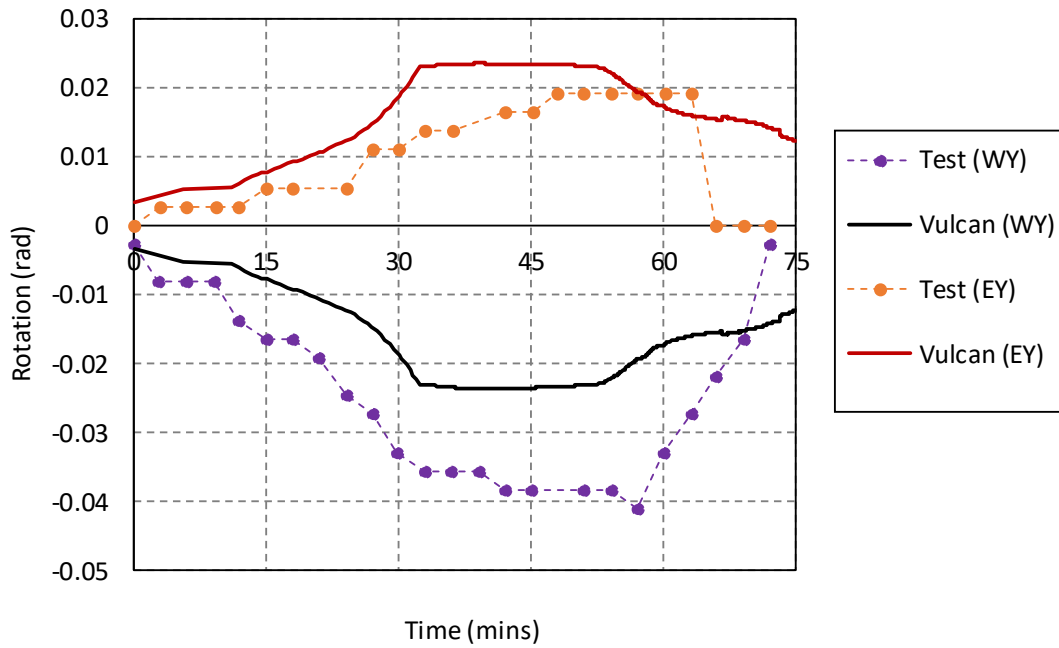


Figure 17. Rotation across beam-ends comparisons between the test and Vulcan modelling

The comparison of the total tensile loads on four No. 4 reinforcing bars between the test and Vulcan modelling is shown in Figure 18. It can be seen that the rebars are mainly at high tensile force until approximately 55 minutes from ignition, when they start to experience low compressive force. During the analysis, it was found that the rebar force was extremely sensitive to the combination of beam-end axial force and rotation. It can be seen that, even for the symmetric test specimen, the total rebar force varied between the east and west beam-ends. Moreover, in Vulcan modelling, the assumption of the evenly distributed stiffness of 36 kN/mm for the supporting springs induces unrealistic axial restraint conditions, as stated above. This changes the ratio of the beam-end axial force and rotation. Although the peak point of the rebar tension force appears earlier than those in the test, overall the Vulcan modelling gives a satisfactory tendency and range of the total rebar forces.

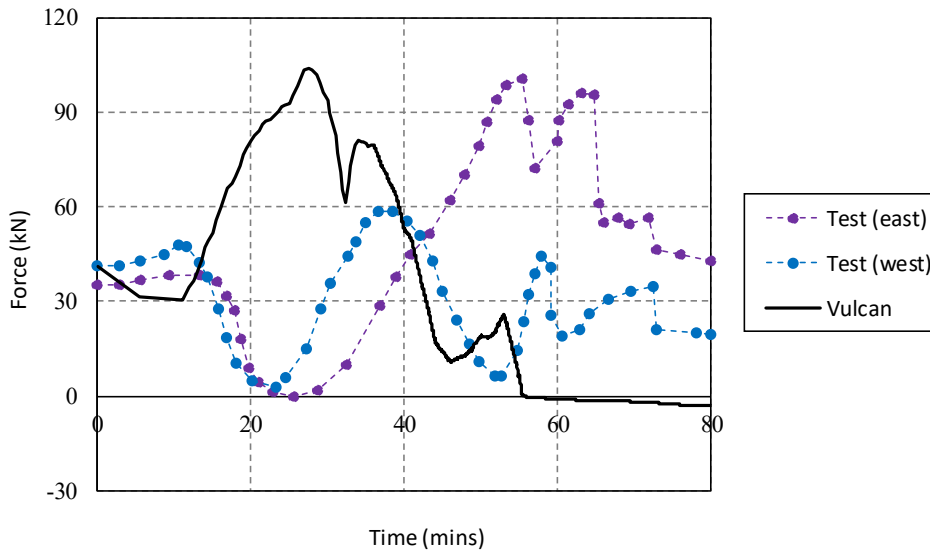


Figure 18. Total tensile loads on No. 4 reinforcing bars comparison between the test and Vulcan modelling

3 Comparison between the composite beam and a bare-steel beam

In this section, the FE modelling results for a bare-steel beam and the composite beam in the NIST composite beam CB-SP-SC test [28, 29] are compared in order to investigate the influence of the continuous concrete slab on the beam deflection and on the beam-end axial force, as well as on the connection bolt row force distributions. The only difference between the two models is that the concrete slab is not modelled for the bare-steel beam model.

The mid-span deflections and the axial force responses of the compared beams are shown in Figure 19 and Figure 20, respectively. Again, the axial force is the overall axial force of the nine supporting springs at one end of the beam. The blue lines represent the results of the bare-steel beam, and the red lines represent the results of the composite beam. It can be seen that the mid-span deflection of the bare-steel beam is significantly higher than that of the composite beam, as the stiffness of the bare-steel beam is lower than that of the composite beam. The analysis of the bare-steel beam terminates at 42 minutes when the

connection bolt rows fracture. The maximum axial compression force of the bare-steel beam is 800kN, which is lower than that of the composite beam (1050kN). This is because the expansion of concrete flange in the composite beam also contribute to the axial compression force.

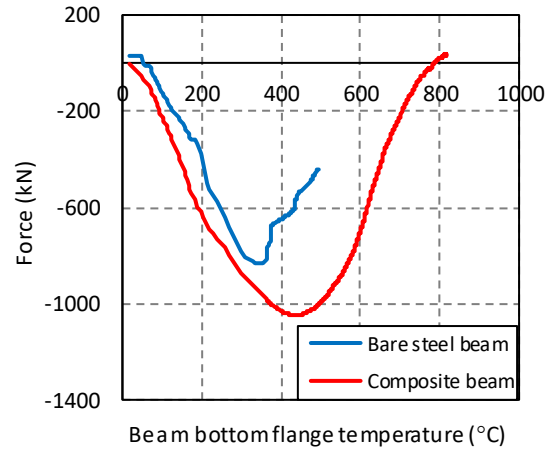
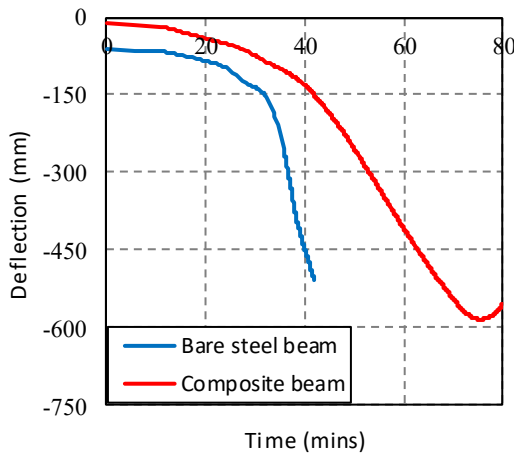


Figure 19. Mid-span deflection comparison between the bare-steel beam and the composite beam

Figure 20. Overall axial force comparison between the bare-steel beam and the composite beam

The comparisons of the axial forces of the connection bolt rows between bare-steel and composite beams are shown in Figure 21. It can be seen that the three bolt rows of the composite beam are all under compression during the analysis. Whereas, the first bolt row of the bare-steel beam is under tension until 18 minutes. After experiencing a compression period up to 35 minutes, the 1st bolt row is under tension again until eventually, the 1st bolt row fractures due to bolt shear failure at 42 minutes. The 2nd bolt row also experiences a small period of tension in the initial phase of loading, and is under tension again after 38 minutes. The 3rd bolt row is under compression for the whole analysis period. It is worth noting that it was observed during the analysis that, after the first bolt row fractured after 42 minutes, the 2nd and 3rd bolt rows

reached their ultimate tensile strengths and fractured in sequence. The axial forces of the 2nd and 3rd bolt rows shown in Figure 21 did not capture this process because the static solver in Vulcan only captures the results when static force equilibrium is reached; the bolt row fracture in sequence process was not a static process. From Figure 21 (d) it can be seen that the bottom flange of the bare-steel beam resists a higher value of compression force than that of the composite beam, when it contacts the column. This helps prevent the connection bolt rows of the bare steel beam from failing under compression force.

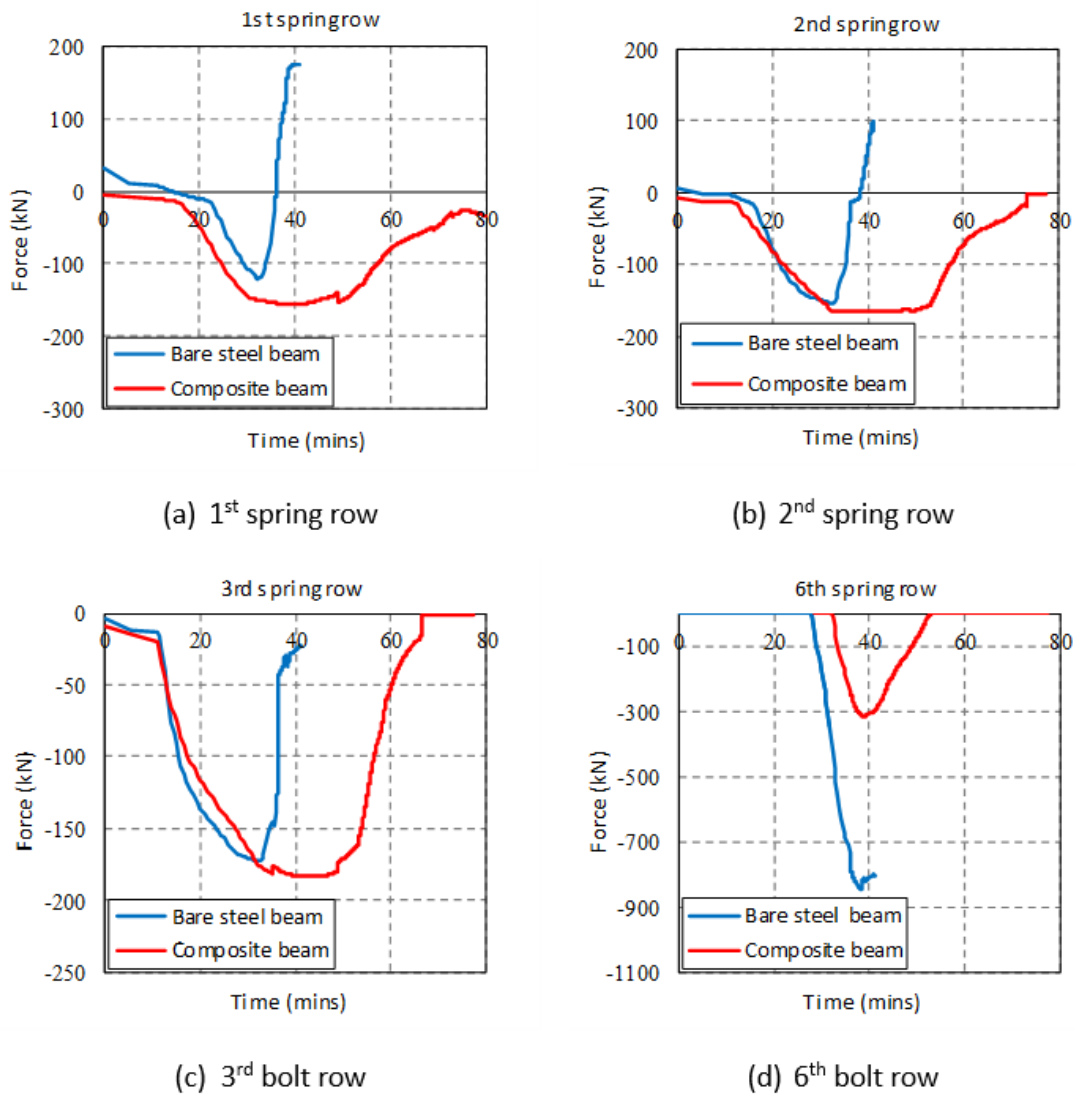


Figure 21. Comparison of the axial forces of the connection springs between bare-steel beam and composite beam: (a) 1st spring row; (b) 2nd spring row; (c) 3rd spring row, and (d) 6th spring row

4 Parametric studies

In this section, parametric studies are carried out on the validated composite beam model to study the influence of key parameters on the behaviour of the composite beams and the connections. The key parameters investigated include the axial restraint stiffness of the composite beam and the reinforcement ratio. During the parametric studies only the investigated parameters vary, while all the other modelling

conditions remain identical to those in the model for the NIST composite beam CB-SP-SC test [28, 29] test in Section 3.

4.1 Effect of axial restraint stiffness

The axial restraint stiffness, which represents the restraint from the surrounding structure in a real building, plays an important role in the behaviour of the composite beam and its beam-end connections. In this study, the total stiffnesses of the axial restraint springs have been selected to be zero, 90kN/mm, 180kN/mm and 1800kN/mm, which are evenly distributed between the five supporting springs at the beam ends. The mid-span deflections and axial force responses of the composite beams are shown in Figures 22 and 23. The axial force of a composite beam was obtained by summing the axial reaction forces of the nine supporting springs at the same end of the composite beam (see Figure 13). It can be seen that the axial restraint stiffness has negligible influence on the mid-span deflection of the selected composite beams. The axial force of the composite beams increases with the increase of axial restraint stiffness. When the axial restraint stiffness is zero, the axial force of the composite beam is zero (see the blue line). The maximum axial force of the composite beam occurs when its bottom flange temperature is between 400 °C and 500 °C. Catenary action starts when the axial forces of the composite beams change from compression to tension. This time is not highly influenced by the axial restraint stiffness. Moreover, as the occurrence of catenary action is related to the beam mid-span deflection [8], the negligible influence of axial restraint stiffness on the beam mid-span deflection also demonstrates its minor influence on the occurrence of catenary action.

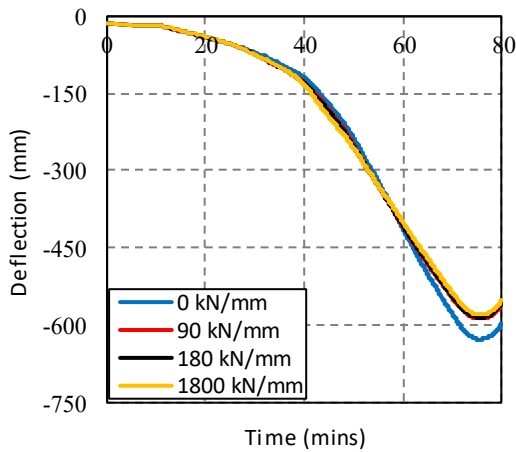


Figure 22. Mid-span deflections of the composite beams with different axial restraint stiffness

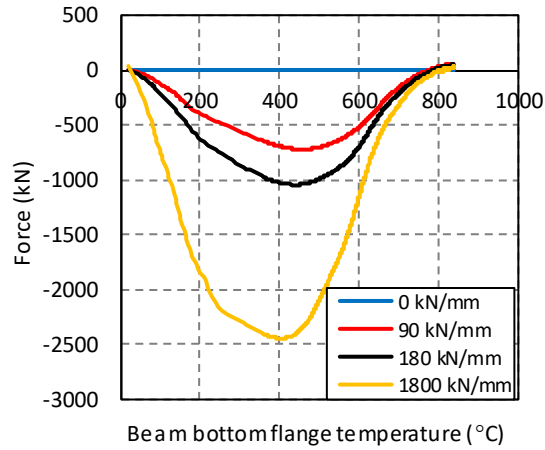


Figure 23. Overall axial forces of the composite beams with different axial restraint stiffness

The axial force of the connection is shown in Figure 24. It was obtained by extracting the axial reaction force of the connection springs at the beam end. It can be seen that when the axial restraint stiffness is zero, the connection is under compression force. This compression force is caused by the restraint from expansion by the columns that are directly linked with the composite beam. The connection axial forces increase with the increase of the axial restraint stiffness, but less rapidly compared with the overall beam axial force shown in Figure 23. The axial forces of the connection bolt rows with different axial restraint stiffness are shown in Figure 25. The 1st to the 3rd spring rows represent the 1st to the 3rd bolt rows. The 6th spring row represents the beam bottom flange getting in contact with the column. The 7th spring row represents the force within the reinforcement when the concrete flange is under tension, and the force within the concrete and reinforcement when the concrete flange is under compression.

It can be seen that the three bolt rows are all under compression force during the analysis. The compression

forces of the 2nd and the 3rd bolt rows are nearly zero in the late heating period, which shows that these two bolt rows become detached from the bolt hole edges when the beam ends rotate anti-clockwise. The alteration of axial restraint stiffness has little influence on the 1st and 2nd bolt row forces. The maximum force of the 3rd bolt row increases by approximately 30% when the axial restraint stiffness increases by 10 times (to 1800 kN/mm). When the axial restraint stiffness increases, the majority of additional axial force is withstood by the steel beam bottom flange that contacts the column, as shown in Figure 25 (d). The forces of the 6th spring decrease after approximately 40 minutes as the beam end rotation decrease, and the 6th springs start to be within the unloading curves. For the force within the rebars or welded fabric shown in Figure 25 (e), when the axial restraint stiffness is zero, the rebar force is initially similar to those when the axial restraint stiffness is 90kN/mm and 180kN/mm. The rebar force starts to decrease more rapidly than those with the axial restraint stiffness to be 90kN/mm and 180kN/mm, at the time of approximately 32 minutes. This is because with similar axial connection force to the other two beams, the rebar force has to start to reverse to compression due to force equilibrium, while for the beams with axial restraint of 90kN/mm and 180kN/mm, the compression forces are resisted by the beam bottom flange in contact with the column. When the axial restraint stiffness is 1800kN/mm, the 7th spring is mainly under compression due to the excessive compression force produced in the connection.

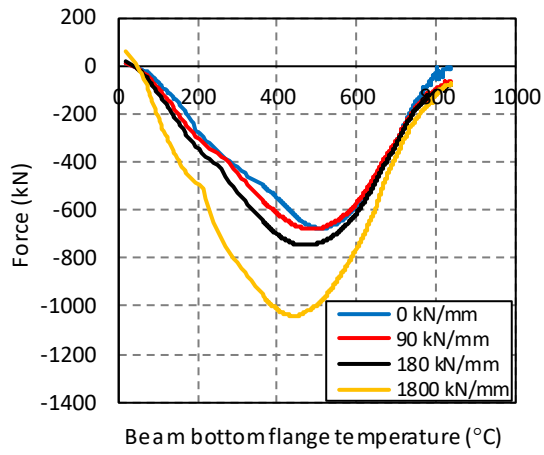
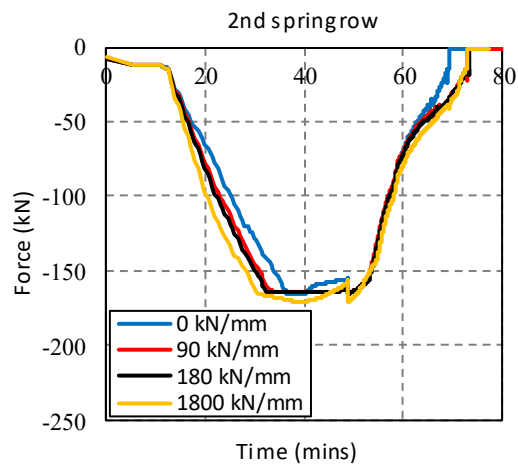
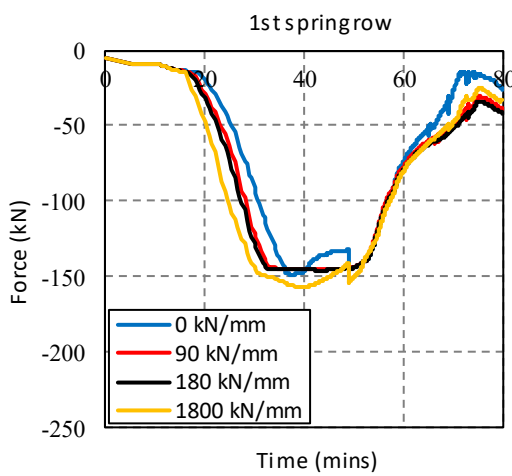
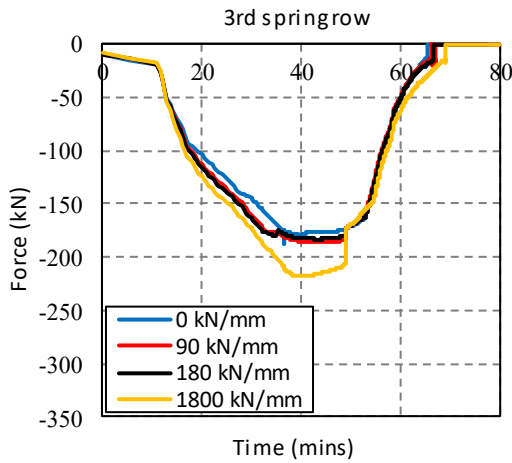


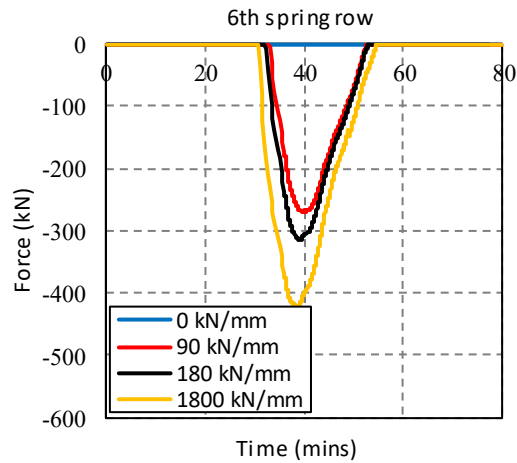
Figure 24. Axial force of the connections with different axial restraint stiffness



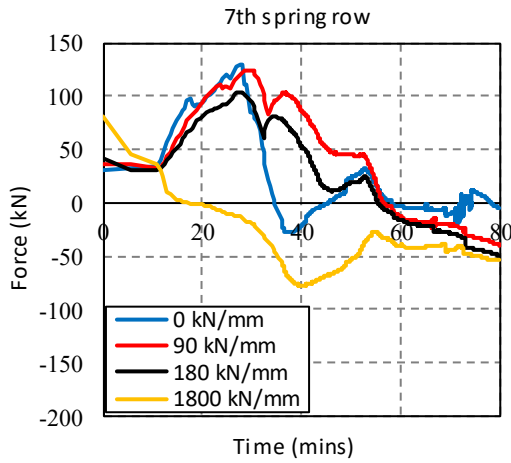
(a) 1st spring row



(b) 2nd spring row



(c) 3rd spring row



(d) 6th spring row

(e) 7th spring row

Figure 25. Axial forces of the connection springs with different axial restraint conditions: (a) 1st spring row; (b) 2nd spring row; (c) 3rd spring row; (d) 6th spring row, and (e) 7th spring row

4.2 Effect of reinforcement ratio

In this section, the effect of reinforcement ratio on the deflections and axial forces of the composite beams, as well as on the rebar force, the connection bolt row force distribution and the forces withstood by the beam bottom flange, will be investigated. The reinforcement ratio in the NIST composite beam CB-SP-SC test

[28, 29] was $61\text{mm}^2/\text{m}$ without accounting for the rebars embedded at the beam ends. In this section, the selected reinforcement ratios represent 0.5, 1.0, 5.0 and 10.0 times the reinforcement ratio from experiments [28, 29]. The other conditions of the analysed beams are identical. The mid-span deflections and axial force responses of the composite beams are shown in Figures 26 and 27, respectively. It can be seen that the beam mid-span deflection increases with decrease of reinforcement ratio. The overall compression force of the beam also decreases with increase in the reinforcement ratio. This is because a higher reinforcement ratio provides higher restraint to the thermal expansion of the slab from expanding. However, when the bottom-flange temperature is approximately 650°C , the beam overall compression forces increase with the increase of the reinforcement ratio. It can be seen that for beams with reinforcement ratios of $305\text{mm}^2/\text{m}$ and $610\text{mm}^2/\text{m}$, the beams do not experience catenary action at the end of heating. The connection axial forces with different reinforcement ratios are shown in Figure 28. For the same reason, the beam overall compression forces decrease with the increase of the reinforcement ratio. However, at the end of heating period with the temperature higher than 780°C , the deflection of the beam with reinforcement ratio of $610\text{mm}^2/\text{m}$ is between those with reinforcement of $31\text{mm}^2/\text{m}$, $61\text{mm}^2/\text{m}$ and $305\text{mm}^2/\text{m}$. The beam deflections are not in either the ascending order or the descending order with the reinforcement ratio. This may be because it is assumed that the stiffness of the ten springs that support the composite beam are assumed to be identical (36kN/mm). Whereas, the actual stiffness distribution provided by the supporting column is unknown. There may be some discrepancy between the FE results and the real overall axial forces of the connections.

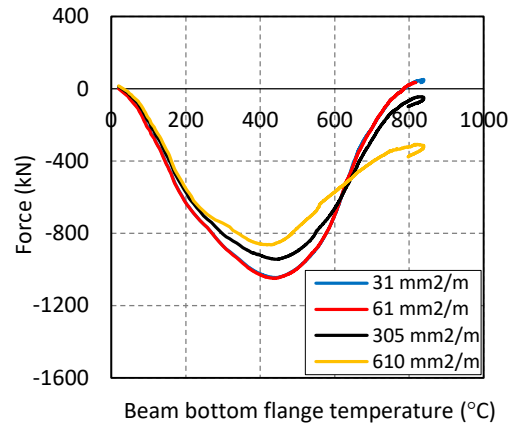
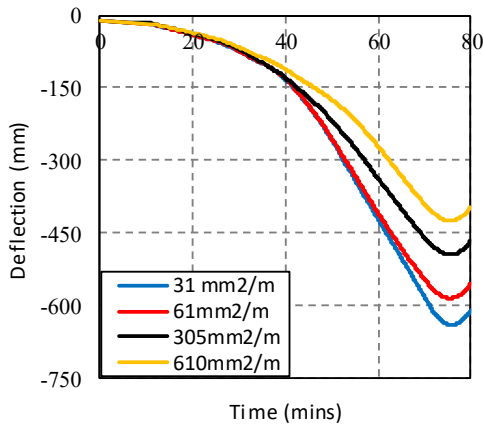


Figure 26. Mid-span deflections of the composite beams with difference reinforcement ratios

Figure 27. Overall axial forces of the composite beams with difference reinforcement ratios

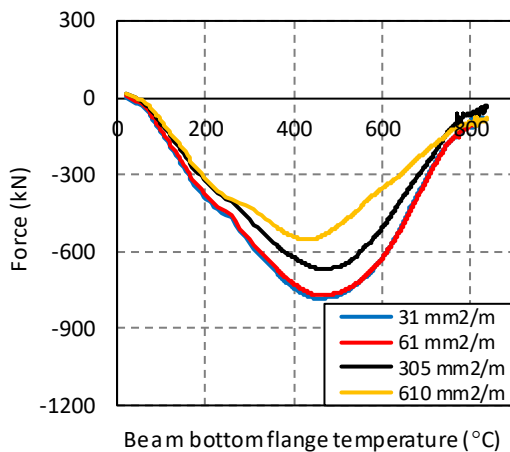


Figure 28. Axial force of the connections with difference reinforcement ratios

The axial forces of the connection bolt rows with different reinforcement ratios are shown in Figure 29. The 1st to the 3rd spring rows represent the 1st to the 3rd bolt rows. The 6th spring row represents the beam bottom flange in contact with the column. The 7th spring row represents the force of the rebars when the concrete

flange is under tension, and the force within the concrete and rebars when the concrete flange is under compression.

It can be seen that the three bolt rows are all under compression during the analysis. The variations of the reinforcement ratios have negligible influence on the bolt-row force distribution, except that the compression force of the 1st bolt row for the reinforcement ratio of 610 mm²/m is approximately 20% less than in the other connections from the time of 48 minutes. The compression force withstood by the beam bottom flange (shown in Figure 29 (d)) decreases with the increase of the reinforcement ratio. This is because the beam with a higher reinforcement ratio rotates less, and therefore the beam bottom flange contacts the column less positively. For the forces within the reinforcement shown in Figure 29 (e), the rebars were pulled out for the beams with reinforcement ratios of 31mm²/m and 61mm²/m. This can be identified by the unchanged spring axial force between the times of 10 and 33 minutes. For the beams with reinforcement ratios of 305mm²/m and 610mm²/m, the rebars were not pulled out, but resisted similar tensile force for both beams. Therefore, it can be concluded that when insufficient bond force can be provided to the reinforcing bars, they will be pulled out. The rebar tensile forces are limited by the reinforcement ratio. When sufficient bond force can be provided to the rebars, they resist similar forces if the reinforcement ratio is the single variable differentiating the composite beams.

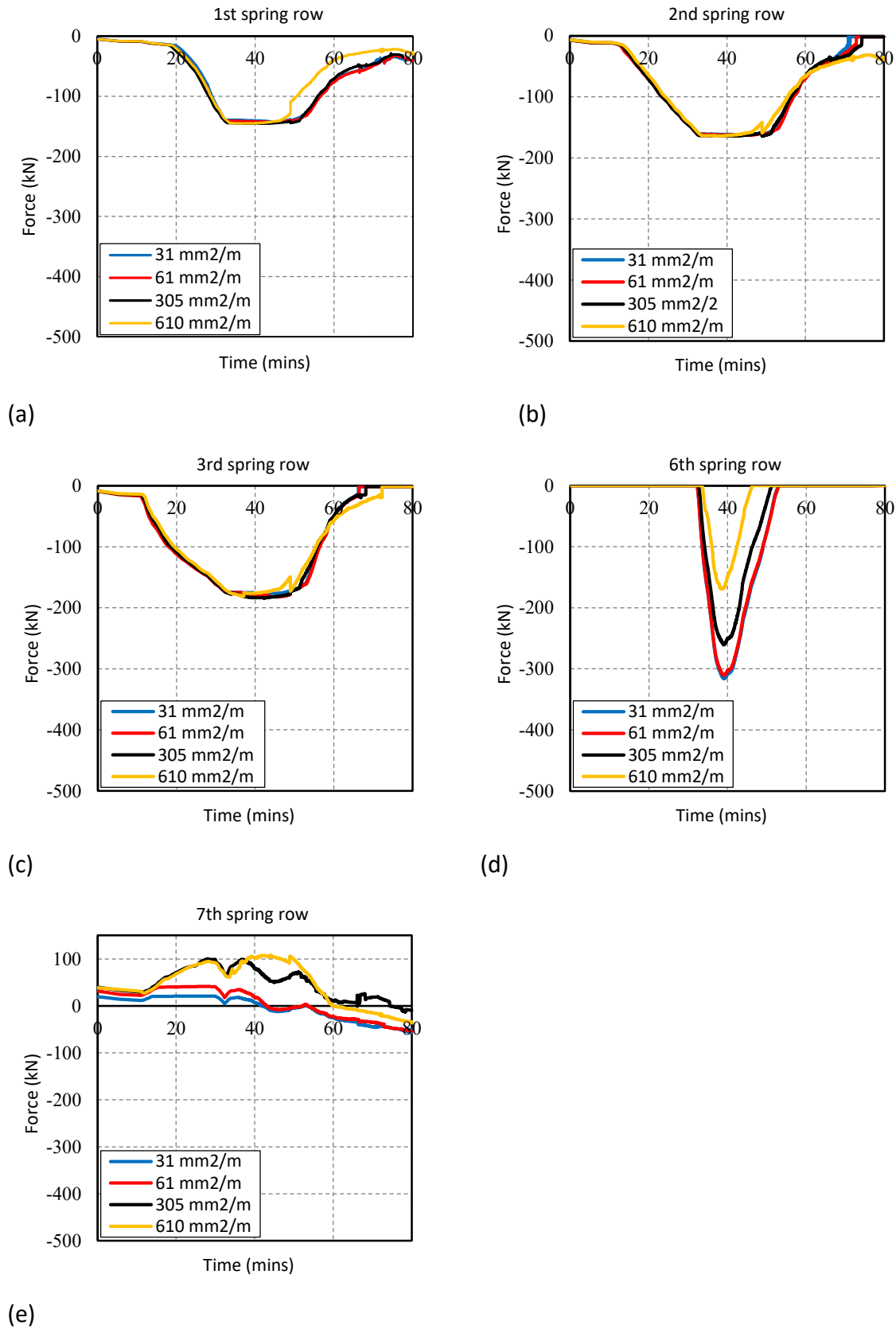


Figure 29. Axial forces of the connection springs under different reinforcement ratios: (a) 1st spring row; (b)

2nd spring row; (c) 3rd spring row; (d) 6th spring row, and (e) 7th spring row

5 Conclusions

In this study a component-based composite fin-plate connection model, which considers the slab continuity of a composite beam, has been proposed. The component-based composite fin-plate connection model is composed of nonlinear springs, which represent the behaviour of the concrete flange containing rebars, the bolt rows and the beam bottom flange in contact with the column. Each spring is able to deal with deformation reversal, which commonly happens to beam-end connections at high temperatures. The component-based composite fin-plate connection element has been implemented into the 3D FE analysis software Vulcan.

The composite fin-plate connection element has been verified against a range of tests. The comparisons between the Vulcan modelling results and the tests show that the proposed component-based model can efficiently represent the behaviour of the composite fin-plate connections. The software Vulcan, together with the newly implemented composite fin-plate connection element, is a reliable tool to enable the performance-based FE modelling of full-scale composite structures with fin-plate connections under fire conditions.

Comparisons have been made between a bare-steel beam with steel fin-plate connection and a composite beam with the proposed component-based composite fin-plate connection under identical loading and heating conditions. It has been found that the mid-span deflection of the bare-steel beam is larger than that of the composite beam. The bare-steel beam overall axial force measured at the beam end is smaller than that of the composite beam. The 1st and 2nd bolt rows of the bare-steel connection experience tensile force

after 35 and 38 minutes, respectively. The bolt rows eventually fail by bolt shear failure when the spring rows are under tension, in the sequence from the 1st to the 3rd bolt row. The bolt rows of the composite beam are all under compression. No bolt row failure has been found in the composite beam during the analysis. After the beam bottom flange contacts the column, the axial compression force produced in the bare-steel beam bottom flange is larger than that of the composite beam.

The axial restraint stiffness has negligible influence on the deflection of the composite beams. The overall beam axial compression force and the overall axial compression force of the fin-plate connections are larger for the composite beams with higher axial restraint stiffness. The axial restraint stiffness has little influence on the bolt row forces. The main additional axial compression force for the beams with higher axial restraint stiffness is resisted by the concrete flange, as well as by the beam bottom flanges when they contact with the column.

The composite beam mid-span deflection, the connection axial force and the overall beam-end compression force increase with the decrease of reinforcement ratio. However, this situation is reversed for the connection axial force after the beam bottom-flange temperature exceeds 650°C. The reinforcement ratio has negligible influence on the connection bolt row forces. However, the beam bottom flange compression force increases with the decrease of reinforcement ratio. The tensile force resisted by the reinforcements within the concrete flange increase with the increase of reinforcement ratio.

The future work will include the validation of the newly developed composite fin-plate connection against more complex full-scale composite structures under fire conditions.

Appendix

Table A. 1. Parameters for the plate bearing model [35]

	Plate in bearing									Bolt in shear
T (°C)	In tension with $e_2 \geq 2d_b$ or in compression									
	In tension with $e_2 \leq 2d_b$									
	$d_b \leq 20\text{mm}$			$d_b > 20\text{mm}$						
	Ω	Ψ	Φ	Ω	Ψ	Φ	Ω	Ψ	Φ	Ω_s
20	145	1.74	0.009	250	1.7	0.008	250	1.7	0.011	2.5
100	180	2	0.008	220	1.7	0.008	220	1.7	0.011	2.8
200	180	2	0.008	220	1.7	0.008	220	1.7	0.011	2.0
300	180	2	0.008	220	1.7	0.008	220	1.7	0.011	2.2
400	170	2	0.008	200	1.7	0.008	200	1.7	0.009	2.0
500	130	2	0.008	170	1.7	0.008	170	1.7	0.007	2.0
600	80	2	0.008	110	1.7	0.008	110	1.7	0.0055	1.3
700	45	2	0.008	40	1.7	0.007	40	1.7	0.0055	0.6
800	20	1.8	0.008	20	1.7	0.007	20	1.7	0.001	0.7

References

- [1] Burgess I, Davison JB, Dong G, Huang S-S. The role of connections in the response of steel frames to fire. *Structural Engineering International*. 2012;22:449-61.
- [2] National Institute of Standards and Technology. Final report on the collapse of the World Trade Center towers: US Department of Commerce, Technology Administration; 2005.
- [3] CEN. Eurocode 1993-1-8: Eurocode 3: Design of steel structures. Part 1-8: Design of joints.: European Committee for Standardization; 2005.

- [4] CEN. Eurocode 3: Design of Steel Structures-Part 1-2: General Rules-Structural Fire Design. 2007.
- [5] Wald F, Da Silva LS, Moore D, Lennon T, Chladna M, Santiago A, Benes M, Borges L. Experimental behaviour of a steel structure under natural fire. *Fire Safety Journal*. 2006;41:509-22.
- [6] Huang Z, Burgess I, Plank R. Three-dimensional Modelling of Two Full-scale Fire Tests on a Composite Building. *Proceedings of the Institution of Civil Engineers-Structures and Buildings*. 1999;134:243-55.
- [7] Dai X, Choe L, Fischer E, Clifton C. Thermal response and capacity of beam end shear connections during a large compartment fire experiment. *Proceedings of the 11th International Conference on Structures in Fire*. 2020; 386-397.
- [8] Yin Y, Wang Y. Analysis of catenary action in steel beams using a simplified hand calculation method, Part 1: theory and validation for uniform temperature distribution. *Journal of Constructional Steel Research*. 2005;61:183-211.
- [9] Yin Y, Wang Y. Analysis of catenary action in steel beams using a simplified hand calculation method, Part 2: validation for non-uniform temperature distribution. *Journal of Constructional Steel Research*. 2005;61:213-34.
- [10] Wang Y, Burgess I, Wald F, Gillie M. *Performance-based fire engineering of structures*: CRC press; 2012.
- [11] Vulcan Solution Ltd. Vulcan software package. 2005. <http://vulcan-solutions.com/www/>
- [12] Huang Z, Burgess IW, Plank RJ. 3D Modelling of Beam-columns with General Cross-sections in Fire. Paper S6-5, Third International Workshop on Structures in Fire, Ottawa, Canada 2004. p. 323-34.
- [13] Huang Z, Burgess IW, Plank RJ. Three-dimensional analysis of reinforced concrete beam-column

structures in fire. *Journal of Structural Engineering*. 2009;135:1201-12.

[14] Huang Z, Burgess IW, Plank RJ. Three-dimensional analysis of composite steel-framed buildings in fire. *Journal of structural engineering*. 2000;126:389-97.

[15] Huang Z, Burgess IW, Plank RJ. Effective stiffness modelling of composite concrete slabs in fire. *Engineering Structures*. 2000;22:1133-44.

[16] Huang Z, Burgess IW, Plank RJ. The influence of shear connectors on the behaviour of composite steel-framed buildings in fire. *Journal of Constructional Steel Research*. 1999;51:219-37.

[17] Block FM, Burgess IW, Davison JB, Plank RJ. The development of a component-based connection element for endplate connections in fire. *Fire Safety Journal*. 2007;42:498-506.

[18] Dong G, Burgess I, Davison J. Component-based element for endplate connections in fire'. *Proc ASFE*. 2011:195-200.

[19] Sarraj M. The behaviour of steel fin-plate connections in fire: University of Sheffield; 2007.

[20] Systèmes D. Abaqus analysis user's guide. Solid (Continuum) Elements. 2014;6:2019.

[21] Hu G. Behavior of beam shear connections in steel buildings subject to fire: the University of Texas at Austin; 2011.

[22] Yu H, Burgess I, Davison J, Plank R. Experimental investigation of the behaviour of fin-plate connections in fire. *Journal of Constructional Steel Research*. 2009;65:723-36.

[23] Taib M. The performance of steel framed structures with fin-plate connections in fire: University of Sheffield; 2012.

- [24] Selden KL, Fischer EC, Varma AH. Experimental investigation of composite beams with shear connections subjected to fire loading. *Journal of Structural Engineering*. 2016;142:04015118.
- [25] Fischer EC, Selden KL, Varma AH. Experimental evaluation of the fire performance of simple connections. *Journal of Structural Engineering*. 2017;143:04016181.
- [26] Fischer EC, Varma AH. Fire resilience of composite beams with simple connections: Parametric studies and design. *Journal of Constructional Steel Research*. 2017;128:119-35.
- [27] Yotsumoto N, Hirahisma T, Toyoda K. Evaluation of the fire performance of unprotected composite beams with fin-plate joints. 2020.
- [28] Ramesh S, Choe L, Seif M, Hoehler M, Grosshandler W, Sauca A, Bundy M, Luecke W, Bao Y, Klegseth M, Chen G, Reilly J, Glisic B. Compartment Fire Experiments on Long-Span Composite-Beams with Simple Shear Connections Part 1: Experimental Design and Beam Behavior at Ambient Temperature: US Department of Commerce, National Institute of Standards and Technology; 2019.
- [29] Choe LY, Ramesh S, Hoehler MS, Seif MS, Bundy MF, Reilly J et al. Compartment Fire Experiments on Long-Span Composite-Beams with Simple Shear Connections, Part 2: Test Results. 2019.
- [30] Agency FEM. World Trade Center building performance study: Data collection, preliminary observations, and recommendations: Government Printing Office; 2002.
- [31] Choe L, Ramesh S, Grosshandler W, Hoehler M, Seif M, Gross J et al. Behavior and limit states of long-span composite floor beams with simple shear connections subject to compartment fires: experimental evaluation. *Journal of Structural Engineering*. 2020;146:04020088.

- [32] Sezen H, Setzler EJ. Reinforcement slip in reinforced concrete columns. *ACI Structural Journal*. 2008;105:280.
- [33] Eurocode 4: Design of composite steel and concrete structures-Part 1-2: General Rules-Structural Fire Design 2008.
- [34] Quan G, Huang S-S, Burgess I. The behaviour and effects of beam-end buckling in fire using a component-based method. *Engineering Structures*. 2017;139:15-30.
- [35] Sarraj M, Burgess I, Davison J, Plank R. Finite element modelling of steel fin-plate connections in fire. *Fire Safety Journal*. 2007;42:408-15.
- [36] Richard RM, Abbott BJ. Versatile elastic-plastic stress-strain formula. *Journal of the Engineering Mechanics Division*. 1975;101:511-5.
- [37] Ramberg W, Osgood W. Description of stress–strain curves by 3 parameters. Technical Report 902: National Advisory Committee for Aeronautics; 1943.
- [38] BS EN 1090, Execution of steel structures and aluminium structures, Part 2: Technical requirements for steel structures. 2008.
- [39] Vulcan Solutions Ltd. Technical User Manual of Vulcan (Academic version). 2nd Edition. 2012.
- [40] Renner A. The effect of strain-rate on the elevated-temperature behaviour of structural steel. Research dissertation, University of Sheffield. 2005.
- [41] Hu Y, Davison J, Burgess I, Plank R. Comparative study of the behaviour of BS 4190 and BS EN ISO 4014 bolts in fire. *Proceedings of 3rd international conference on steel and composite structures*; 2007.